

## Wetting of polymer liquids: Monte Carlo simulations and self-consistent field calculations

This article has been downloaded from IOPscience. Please scroll down to see the full text article.

2003 J. Phys.: Condens. Matter 15 R609

(<http://iopscience.iop.org/0953-8984/15/19/201>)

View [the table of contents for this issue](#), or go to the [journal homepage](#) for more

Download details:

IP Address: 171.66.16.119

The article was downloaded on 19/05/2010 at 09:37

Please note that [terms and conditions apply](#).

## TOPICAL REVIEW

# Wetting of polymer liquids: Monte Carlo simulations and self-consistent field calculations

Marcus Müller<sup>1</sup> and Luis González MacDowell<sup>2</sup><sup>1</sup> Institut für Physik, WA331, Johannes Gutenberg Universität, D-55099 Mainz, Germany<sup>2</sup> Departamento de Química Física, Facultad de Ciencias Químicas, Universidad Complutense, 28040 Madrid, Spain

Received 22 January 2003

Published 6 May 2003

Online at [stacks.iop.org/JPhysCM/15/R609](http://stacks.iop.org/JPhysCM/15/R609)**Abstract**

Using Monte Carlo simulations and self-consistent field (SCF) theory we study the surface and interface properties of a coarse grained off-lattice model. In the simulations we employ the grand canonical ensemble together with a reweighting scheme in order to measure surface and interface free energies and discuss various methods for accurately locating the wetting transition. In the SCF theory, we use a partial enumeration scheme to incorporate single-chain properties on all length scales and use a weighted density functional for the excess free energy. The results of various forms of the density functional are compared quantitatively to the simulation results. For the theory to be accurate, it is important to decompose the free energy functional into a repulsive and an attractive part, with different approximations for the two parts.

Measuring the effective interface potential for our coarse grained model we explore routes for controlling the equilibrium wetting properties. (i) Coating of the substrate by an oxide layer gives rise to a subtle interplay between short-range and long-range forces, which may stabilize a film of mesoscopic thickness or result in the formation of nano-droplets. (ii) Coating the substrate with a polymer brush, we observe second-order wetting transitions at intermediate grafting densities, while the wetting transition is of first order at low and high grafting densities. In the latter limit, polymers of the same chemical structure as the brush do not wet the surface (autophobicity). (iii) Surface pattern (stripes) might give rise to unusual adsorption properties, which are related to morphological transitions. We relate our findings to experiments and discuss perspectives and limitations of the computational methods.

(Some figures in this article are in colour only in the electronic version)

**Contents**

1. Introduction	610
2. Phenomenological description	611

3. Model and Monte Carlo technique	615
3.1. Coarse-grained bead-spring model	615
3.2. Monte Carlo technique	617
3.3. Bulk and interface properties	618
4. Self-consistent field calculations	622
4.1. General formalism	622
4.2. Choice of the free energy densities and weighting functions	625
4.3. Related theoretical approaches	630
4.4. Comparison between SCF calculations and MC simulations	631
5. Wetting on a planar surface	635
5.1. Accurately locating a first-order wetting transition by computer simulations	635
5.2. Comparison between MC simulations and SCF calculations	640
6. Interplay between short-range and long-range interactions	640
7. Wetting on a polymer brush	644
8. Patterned surfaces	648
9. Summary and outlook	649
Acknowledgments	650
References	651

## 1. Introduction

The stability of thin polymer films has attracted abiding interest. Thin polymer films find ubiquitous technological applications (e.g. as dielectric layers, protective coatings, adhesives or lubricants). One key issue is the thermodynamic stability of a thin film: will the film form a stable homogeneous layer on a substrate or will it break up into droplets?

Consequently, much basic research has been directed towards understanding the wetting properties of polymers [1]. Apart from the practical interest, the use of polymers to study the thermodynamic properties of thin films has additional advantages:

- (i) The vapour pressure of long polymers is vanishingly small in comparison to small molecules. Therefore there are very little evaporation effects when a polymer film is in contact with air.
- (ii) Polymers offer much control over surface properties. Changing the length of the polymers or grafting some polymers to the surface one can modify the wetting properties without changing the interaction between segments. This offers ample ways to fine-tune the wetting behaviour.

Typically the width of the interface between a polymer melt and a substrate or a melt and its vapour is of the order of the statistical segment length and, as a consequence, details of the chain architecture and the arrangement of the polymers on the monomer scale significantly influence surface and interface tensions. The latter quantities, in turn, determine macroscopic properties like the contact angle of droplets or the work of adhesion. For a quantitative prediction of such properties, we must consider two different problems. On the one hand, we require an accurate description of the interaction between the chemical constituents of the system; on the other hand, we require a computational scheme that will allow for the calculation of mesoscopic properties (e.g. orientation of the molecules, thickness of wetting layers or free energy cost of surfaces) from knowledge of the detailed chemical description. We will address only the latter problem.

Although considerable theoretical effort has been devoted to polymers at hard surfaces (cf, e.g., [2]), there have been comparatively few studies on situations where attractive

interactions play an important role. Besides their practical relevance, attractive surfaces pose a challenge to computational methods. In the presence of attractive interactions the surface and interfacial free energies are a result of a subtle balance between the strong but short-range repulsions (hard core) and weaker but longer-range attractions. Both simulations and theory have to determine the free energies with a rather high accuracy to predict wetting properties, and this is not a trivial task.

In this review we focus on the static equilibrium properties of a one-component homopolymer liquid at surfaces and interfaces. We use a generic coarse-grained model and uncorrugated surfaces, which attract the fluid via long-range van der Waals interactions. We do not aim at a chemically realistic modelling of a specific polymer, but rather focus on an accurate description within our coarse-grained model, which we expect to provide information about the qualitative behaviour of experimental systems.

This review is arranged as follows: in the next section we give a brief phenomenological description of wetting, which serves to introduce the basic concepts and notation. Then, we describe our computational model and the simulation technique. In the following section we describe the self-consistent field (SCF) calculations. The predictions of the SCF theory for the surface and interface properties are compared to the simulation data in order to gauge the accuracy of the SCF calculations. Our SCF scheme is also placed in context to alternative approaches. In section 5 we discuss various methods to locate the wetting transition in computer simulations and compare our results to the SCF calculations. In the following sections we apply the SCF calculations to study the wetting behaviour of layered substrates and polymer brushes. In section 8 we employ Monte Carlo (MC) simulations in order to illustrate how the wetting behaviour is modified by a patterned substrate. We close with a brief summary and an outlook.

## 2. Phenomenological description

Macroscopic droplets are described by the Young equation [3] which relates the interface tension  $\gamma_{LV}$ , the surface tension of the liquid  $\gamma_{LW}$  and the vapour  $\gamma_{VW}$  to the contact angle  $\Theta$ :

$$\gamma_{LV} \cos \Theta = \gamma_{VW} - \gamma_{LW}. \quad (1)$$

An important feature of Young's equation is that the shape of a macroscopic drop does not depend on its size. This result follows readily from the assumption that the free energy cost of a surface is directly proportional to its area. Such an approximation is good for drops that are macroscopically large. If the size of the drop is of the order of the characteristic length scale of the interfaces, however, the interactions between the substrate and the droplet's liquid–vapour interface, on the one hand, and the free energy cost arising from the curvature of the liquid–vapour interface, on the other, become relevant features which must be taken into account. To a first approximation such effects can be accounted for phenomenologically by augmenting the free energy with a higher order term which is linear in the perimeter of the drop. The coefficient of this contribution is known as the line tension,  $\tau$ . Using the force balance at the contact line and assuming a spherical cap for the shape of the droplet, one obtains Gretz's equation [4]:

$$\gamma_{LV} \cos \Theta = \gamma_{VW} - \gamma_{LW} - \frac{\tau}{R \sin \Theta} \quad (2)$$

where  $R$  denotes the droplet's radius of curvature.

Rather than decomposing the free energy of a droplet into surface and line contributions, we regard the interaction  $g$  between the liquid–vapour interface and the substrate and determine the shape of the droplet by minimizing its free energy. In the following we consider a simple free

energy functional which is sufficient to illustrate the qualitative features [1]. More sophisticated approaches, which are tailored to polymeric liquids, will be discussed in section 4. Moreover, for the sake of simplicity, we will consider the role of the effective interface potential and that related to the drop's curvature separately. That is, let us first consider the effect of having a film of microscopic thickness on top of the substrate, and then study the free energy cost related to the curvature of the interface.

The effective interface potential  $g(l)$  describes the free energy it costs to place the liquid–vapour interface of unit area a distance  $l$  away from the substrate. It is a mesoscopic description of the liquid film on the substrate: on the one hand it abstracts from the details of the interface profile. Rather than describing the detailed packing and enrichment effects of the liquid at the surface and the distortion of the liquid–vapour interface by the presence of the substrate it describes the system by a single parameter,  $l$ , the distance between the substrate and the liquid–vapour interface. On the other hand, the interface potential still retains much more information than just the macroscopic properties like contact angle or liquid–vapour interface tension.

The minimum of the interface potential,  $g_{\min}$ , describes the macroscopic wetting properties. If a stable minimum at some finite film thickness,  $l_0$ , is found, the liquid will not wet the substrate, but will rather form droplets. The contact angle of the droplets is given by [1]

$$\frac{g_{\min}}{\gamma_{LV}} = \cos \Theta - 1. \quad (3)$$

Upon approaching the wetting transition the film thickness diverges. At a second-order wetting transition it grows continuously, while at a first-order wetting transition it jumps discontinuously from a finite microscopic value to a macroscopic value. In the latter case the minimum of  $g(l)$  at finite microscopic thickness becomes metastable for a temperature range above the wetting transition temperature. This gives rise to prewetting: the coexistence of a thin and a thick liquid layer on the substrate at undersaturation. Upon increasing the temperature further, we reduce the difference between the coexisting thin and thick layers. The prewetting coexistence terminates in a prewetting critical point (CP) at  $T_{\text{pwc}}$ .

There are two major contributions to the interface potential [1]:

- The presence of the substrate distorts the liquid–vapour interface. This gives rise to a short-range contribution to the interface potential. As the wings of the interface profile decay exponentially towards the coexistence values on the liquid and vapour side, the short-range contribution has the form

$$\frac{g_{\text{sr}}}{\gamma_{LV}}(l) = ae^{-l/\xi} - be^{-2l/\xi} + ce^{-3l/\xi} + \dots + \quad (4)$$

where  $\xi$  denotes the bulk correlations which sets the characteristic scale of the wings of the interface profile.  $a$ ,  $b$  and  $c$  are phenomenological, temperature-dependent coefficients. As the free energy costs arise from the distortion of the liquid–vapour interface these coefficients are on the order of unity. The calculation of this contribution to the interface potential requires a detailed description of the density profile in the vicinity of the substrate, e.g. as obtained from simulations, SCF theory or density functional calculations. In this phenomenological section we shall illustrate the qualitative behaviour using the specific choice:

$$a = (T - T_{\text{wet}}) + \frac{1}{4} \quad \text{and} \quad b = c = 1. \quad (5)$$

- Another contribution to the interface potential arises from the dispersion forces inside the liquid and between the liquid and the constituents of the substrate. The Hamaker constants

$A_{LL}, A_{LW} > 0$  parametrize the strength of long-ranged attractions between liquid particles and the liquid and the substrate, respectively, i.e.  $V(\mathbf{r}) = -A_{LW}/\pi^2 \rho_l \rho_w |\mathbf{r}|^6$ , where  $\rho_l$  and  $\rho_w$  denote the number densities of liquid and substrate particles, and  $\mathbf{r}$  denotes the distance between the particles. Assuming that the density of the liquid at the wall equals the density of the liquid which coexists with the vapour and approximating the liquid–vapour profile by a sharp kink, one can calculate the energy  $E(l)$  as a function of the film thickness  $l$ :

$$E(l) \equiv -\frac{A_{LW}}{\pi^2} \int_{-\infty < z < 0} d^3 \mathbf{r} \int_{0 \leq z' < l} d^3 \mathbf{r}' \frac{1}{(r - r')^6} - \frac{A_{LL}}{2\pi^2} \int_{0 \leq z < l} d^3 \mathbf{r} \int_{0 \leq z' < l} d^3 \mathbf{r}' \frac{1}{(r - r')^6}. \quad (6)$$

The integrations are extended over the volumes of the materials. The factor 1/2 in the last contribution takes account of the double-counting of interaction pairs in the liquid film. In principle, there are also contributions from the interaction within the substrate, but these do not depend on the thickness  $l$ . Keeping only  $l$ -dependent terms one obtains for the long-range contribution  $g_{\text{vdW}}(l) \equiv E(l)/L^2$

$$g_{\text{vdW}}(l) = \frac{1}{12\pi} \left( -\frac{A_{LL} - A_{LW}}{l^2} \right). \quad (7)$$

More generally, higher-order contributions can be included and one obtains

$$g_{\text{lr}}(l) = \frac{A}{l^2} + \frac{B}{l^3} + \frac{C}{l^4} + \dots + \quad (8)$$

where  $A$ ,  $B$  and  $C$  are phenomenological coefficients. Logarithmic corrections may arise in higher order terms [46].

The above expressions for the interface potential are correct whenever the system is found at coexistence. If, on the other hand, the system is undersaturated, there appears an extra term proportional to  $\Delta\mu l$ , where  $\Delta\mu = \mu - \mu_{\text{coex}} < 0$  denotes the undersaturation of the vapour.

In practice, both short- and long-range interactions are present, but the following qualitative discussion is independent from the range of the interactions. We therefore confine our discussion to the potential of equation (4). Figure 1(a) shows the surface phase diagram for this choice of model potential. It is found that, below  $T_{\text{wet}}$ , the wetting temperature, the vapour may only coexist with a thin film of microscopic size. However, for temperatures above  $T_{\text{wet}}$ , there exists a chemical potential  $\Delta\mu < 0$ , the prewetting chemical potential, at which a thin and a thick film may coexist simultaneously with the vapour. As the chemical potential is increased above the prewetting chemical potential, the thin film becomes unstable and the thick film is favoured. Finally, as coexistence is approached, the film thickness diverges until it reaches macroscopic size.

The effective interface potential describes the interaction between a flat interface and the substrate. More generally one can describe the free energy of a liquid film with surface  $S$  by

$$\mathcal{H}[S] = \int_S dS \{ \gamma_{LV} + \kappa (C - C_s)^2 + \bar{\kappa} G + g(l) \}. \quad (9)$$

The first three contributions describe the free energy of a bent interface. The first term denotes the free energy it takes to create an interface, and it is proportional to the liquid–vapour interface tension. The next terms describe the free energy costs due to bending:  $C$ ,  $C_s$  and  $G$  denote the mean, spontaneous, and Gaussian curvatures, respectively. The coefficients  $\kappa$  and  $\bar{\kappa}$  denote the bending rigidity and the saddle splay modulus of the interface. The last term denotes the interaction between the interface and the substrate.

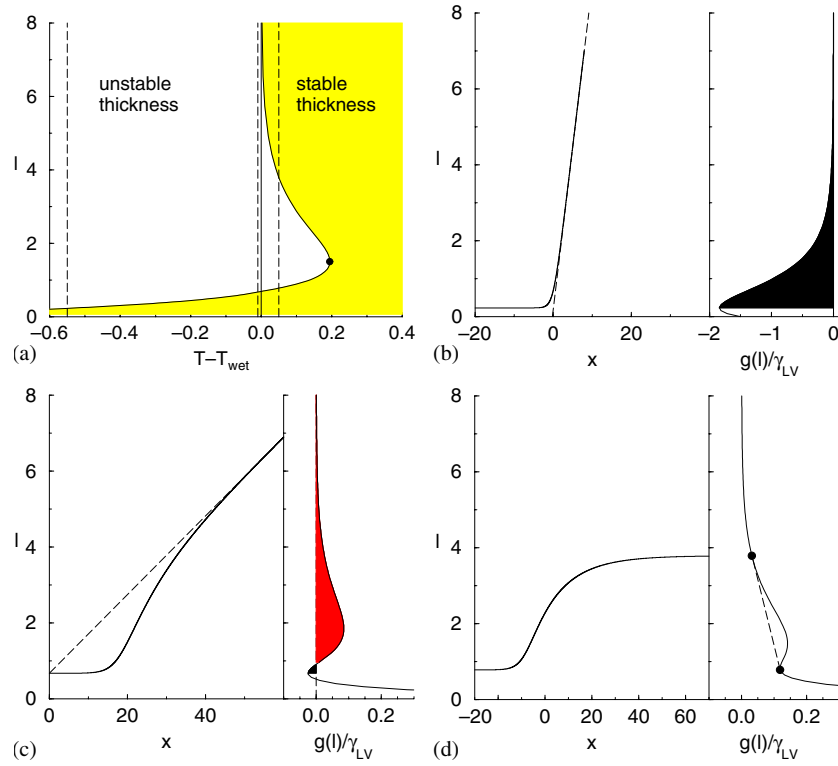


**Figure 1.** (a) Wetting and prewetting. (b) Droplet boundary far below the wetting transition temperature ( $T = T_{\text{wet}} - 0.55$ ). (c) Droplet boundary slightly below the wetting transition temperature ( $T = T_{\text{wet}} - 0.01$ ). (d) Prewetting coexistence above the wetting transition temperature ( $T = T_{\text{wet}} + 0.05$ ). For further explanations, cf the text (from [75]).

If the interface is almost flat, one can describe the local interface position  $l(x, y)$  by the distance of the interface as a function of the two lateral coordinates  $x$  and  $y$  (Monge representation). Furthermore, retaining only leading contributions, one obtains [6, 7]:

$$H[l(x, y)] = \int dx dy \left\{ \frac{\gamma_{LV}}{2} (\nabla l)^2 + g(l) \right\}. \quad (10)$$

The shape of the interface is obtained by minimizing this interface Hamiltonian. In order to give a simple qualitative account, we restrict ourselves in the following to those situations where the distance between the liquid–vapour interface and the wall depends only on a single coordinate  $x$ , while the system is uniform in the other lateral direction. Minimizing the interface Hamiltonian (10) we find the following Euler–Lagrange equation:

$$\gamma_{LV} \frac{d^2 l}{dx^2} = \frac{d}{dl} g(l). \quad (11)$$

When we identify the lateral coordinate  $x$  with time and the distance  $l$  with a particle’s position the Euler–Lagrange equation is equivalent to Newton’s second law for a particle moving in the potential  $-g(l)$ .

In analogy to the mechanical problem, we integrate the Euler–Lagrange equation to obtain (analogous to the conservation of energy in mechanics):

$$\frac{1}{2} \gamma_{LV} \left( \frac{dl}{dx} \right)^2 - g(l) = \text{constant}. \quad (12)$$

The constant is fixed by the initial condition, i.e. thickness of the film in the limit  $x \rightarrow -\infty$ , which we denote  $l_0 = l(x \rightarrow -\infty)$ . The value of  $l_0$  is, however, not arbitrary but imposed as the minimum of  $g(l)$  at the considered chemical potential. Taking this into account, we obtain  $constant = g(l_0)$ . With this boundary condition we can integrate equation (12) again, and obtain for the profile of the film thickness (or particle's trajectory)

$$x = \int_{l_0}^l \frac{\sqrt{\gamma_{LV}} dl'}{\sqrt{2(g(l') - g(l_0))}}. \quad (13)$$

Once the film thickness profiles are known, the line tension for the drop may be calculated (approximately) using the following equation [6, 7]:

$$\tau = \sqrt{2\gamma_{LV}} \int_{l_0}^{\infty} dl' \left\{ \sqrt{g(l') - g(l_0)} - \sqrt{g(\infty) - g(l_0)} \right\}. \quad (14)$$

More accurate expressions for long range interactions have been obtained [8, 9].

The solution for the interface profiles at different temperatures is shown in figures 1(b)–(d). Together with the profiles predicted from equation (13) (full curves), we show the profile that drops would adopt if the contact angle were to be that predicted by Young's equation (broken curves). For each of the chosen temperatures, we also show the interface potential at coexistence (figures 1(b), (c)) and at the prewetting chemical potential (figure 1(d)). The shaded areas of the interface potentials represent the region where the integral of equation (14) has significant contributions. For temperatures well below  $T_{\text{wet}}$ , the line tension is small and negative. Accordingly, the interface profile is almost linear and follows closely that which would be expected from Young's equation almost up to the rim (see figure 1(b)). As we approach the wetting transition temperature  $T_{\text{wet}}$ , however, the line tension changes sign and becomes large and positive. This leads to a profile with a limiting slope far larger than that predicted by Young's equation (figure 1(c)). The shape of the rim of the droplet has been calculated analytically in [8, 9]. For temperatures above  $T_{\text{wet}}$ , the liquid wets the substrate and a macroscopically thick liquid layer is adsorbed on the substrate in contact with a saturated vapour. If the vapour is undersaturated, there will be a coexistence between a thin and a thick liquid layer, the two coexisting states at the prewetting line. The shape of the interface connecting those two states is presented in figure 1(d).

We shall test these phenomenological predictions by MC simulations and SCF calculations for a generic polymeric model. In the next section, we introduce our computational model and provide information about the bulk and interface properties pertinent to the wetting behaviour.

### 3. Model and Monte Carlo technique

#### 3.1. Coarse-grained bead-spring model

We use a standard coarse-grained off-lattice model [10, 11] which incorporates the relevant features of polymeric materials: excluded volume of segments, chain connectivity and an attractive interaction between monomers. The model does not contain information about the chemical structure on the atomistic level, and each monomer in our model should be thought of rather as a small number of chemical repeat units.

The different interactions to which the monomeric units are subjected are illustrated in figure 2(a). Monomeric units interact via a Lennard-Jones (LJ) potential which is cut off at twice the minimum distance and shifted in order to produce a continuous potential. This bead–bead interaction,  $V_{\text{LJ}}(r)$ , is given by

$$V_{\text{LJ}}(r) = 4\epsilon \left\{ \left( \frac{\sigma}{r} \right)^{12} - \left( \frac{\sigma}{r} \right)^6 + \frac{127}{16384} \right\} \quad \text{for } r < r_{\text{max}} \equiv 2 \times 2^{1/6} \sigma. \quad (15)$$

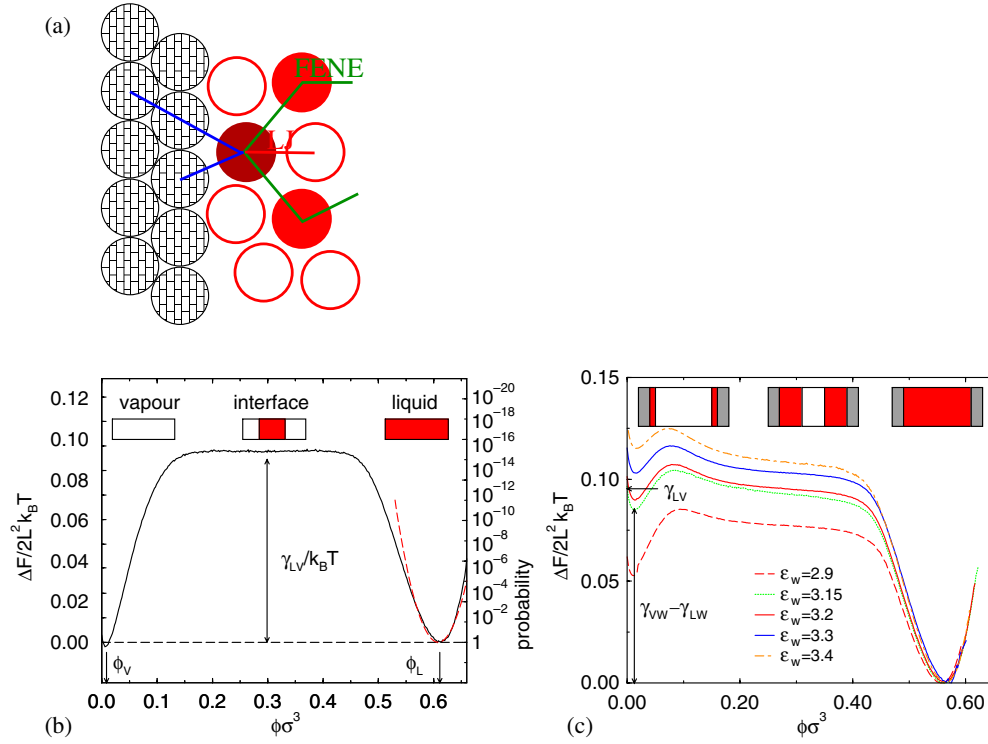


**Figure 2.** (a) Sketch of the interaction in our model system of a polymer liquid in contact with a wall. (b) Illustration of the simulation technique for temperature  $k_B T/\epsilon = 1.68$  and  $\mu_{\text{coex}} = 106.897$ . A cuboidal system geometry  $13.8\sigma \times 13.8\sigma \times 27.6\sigma$  with periodic boundary conditions in all three directions is used. The full curve corresponds to the negative logarithm of the probability distribution  $P(\phi)$  in the grand canonical ensemble. The two minima correspond to the coexisting phases and the arrows on the  $\phi$  axis mark their densities. The height of the plateau yields an accurate estimate for the interfacial tension  $\gamma_{LV}$ . The broken curve is a parabolic fit in the vicinity of the liquid phase employed to determine the compressibility. The typical system configurations are sketched schematically. (c) Free energy as a function of the density of a system, which is confined between walls of attractive strength  $\epsilon_w$ . The grand canonical simulations at  $k_B T/\epsilon = 1.68$  and coexistence chemical potential in the bulk are performed in a geometry  $13.8\sigma \times 13.8\sigma \times 27.6\sigma$ . The curves are shifted such that the free energy of the liquid phase vanishes. The horizontal arrow on the left marks the value of the interfacial tension  $\gamma_{LV}$ , while the vertical arrow marks the difference in the surface tension between the vapour/wall and liquid/wall for  $\epsilon_w = 3.15$ . Typical system configurations are sketched schematically (from [24]).

and  $V_{LJ}$  vanishes for larger distances. In addition to the LJ potential, monomers along a chain interact via a FENE potential:

$$V_{\text{FENE}}(r) = -15\epsilon \left(\frac{R_0}{\sigma}\right)^2 \ln\left(1 - \frac{r^2}{R_0^2}\right) \quad \text{with } R_0 = 1.5\sigma. \quad (16)$$

The parameters are chosen such that the LJ potential between non-bonded segments prefers a distance  $r_{\text{nb}} \approx 1.12\sigma$ , while the most favourable distance between bonded neighbours  $r_{\text{b}} \approx 0.96\sigma$  is slightly smaller. The mismatch between the bonded and non-bonded length scales suppresses long-ranged crystalline order, and the model exhibits glassy behaviour [11] for densities comparable to or larger than the triple point density of the monomer fluid.

Each monomer interacts with the walls via a LJ 9–3 interaction given by

$$V_{\text{wall}}(z) = \epsilon_w \left\{ \left( \frac{\sigma}{z} \right)^9 - \left( \frac{\sigma}{z} \right)^3 \right\} \quad (17)$$

where  $z$  is the distance between a monomer and the wall. This potential mimics the van der Waals interactions between the molecules of the wall and the monomers (cf equation (7)). The parameter  $\epsilon_w$  plays the role of the Hamaker constant. Increasing  $\epsilon_w$  the wall attracts the liquid and eventually the liquid will wet the wall and form a stable homogeneous film.

For computational convenience, we focus on short chains of  $N = 10$  segments and temperature  $k_B T/\epsilon = 1.68$ , where  $k_B$  is Boltzmann's constant and  $T$  is the temperature. If these parameters were mapped onto a realistic polymer model this chain length would correspond to roughly 40 chemical repeat units at a fairly elevated temperature  $T \approx 0.5\Theta \approx 3.7T_g$ , where  $k_B\Theta/\epsilon \approx 3.3$  denotes the reduced  $\Theta$  temperature [12] and  $k_B T_g/\epsilon \approx 0.45$  the reduced glass transition temperature [11]. Under these conditions the density of the vapour phase is negligible, but the density of the liquid (melt) is not too high and allows for an efficient equilibration of the system. For chain length  $N = 10$  the chains' end-to-end distance is  $R_e = 3.66\sigma$ .

### 3.2. Monte Carlo technique

We perform MC simulations in the canonical ensemble to study the detailed profiles of a concentrated polymer solution in contact with a wall and the liquid–vapour interface. This technique is also employed in order to investigate the properties of microscopic droplets. Random local displacements of the individual segments as well as slithering-snake-like motions are used to update the polymer conformations. Typically these MC moves are applied in the ratio 1:1. One MC cycle corresponds to 1 local displacement per monomer and 1 slithering-snake movement per polymer. Every 100 or 5000 MC cycles a configuration is stored for further analysis of the profiles or to analyse the droplet shape, respectively. Typically, we averaged results over 1500 000 MC cycles for each set of parameters.

To determine the phase behaviour or measure the excess free energies of inhomogeneous solutions we simulate in the grand canonical ensemble, i.e. rather than simulating at constant number of particles we fix the chemical potential  $\mu$  of the polymer. In addition to the updates of the polymer conformations (as described above) we perform polymer insertions and deletions via configurational bias [13–15]. The configurational bias scheme utilizes a biased insertion method to ‘grow’ a polymer successively into the system. At each step a small number (typically 25) of segment positions is examined and a position for insertion of the next monomer along the chain is chosen according to its Boltzmann weight. This choice biases the insertion towards non-overlapping/low-energy chain conformations. Once a chain has been grown the bias in the construction is compensated in the MC lottery. Typically, we used systems of size  $13.8\sigma \times 13.8\sigma \times 27.6\sigma$  in the grand canonical simulations.

The grand canonical simulation scheme does not correspond to a realistic dynamics. However, it allows for a much faster equilibration of density fluctuations, which would decay in the canonical ensemble via the slow diffusive motion of the polymers. For instance, the equilibration of the thickness of wetting layers at the surface in the canonical ensemble would require an exchange of polymers between the vapour phase and the liquid layer at the wall via polymer diffusion. In order to act as a particle reservoir, the vapour phase would have to be enormously large to accommodate sufficient polymers to observe the dependence of the wetting layer on the monomer wall interaction.

### 3.3. Bulk and interface properties

The key quantity to monitor in the grand canonical simulations is the probability distribution  $P(\phi)$  of the density. At phase coexistence this distribution exhibits two pronounced peaks, which correspond to the vapour and the liquid phase. The coexistence chemical potential  $\mu_{\text{coex}}(T)$  is fixed by the condition of equal weight in both peaks [16, 17]:

$$\int_0^{\phi^*} d\phi P(\phi) \stackrel{!}{=} \int_{\phi^*}^{\infty} d\phi P(\phi) \quad \text{with } \phi^* = \int_0^{\infty} d\phi P(\phi)\phi. \quad (18)$$

Using histogram extrapolation [18] we can estimate the probability distribution for parameters close to the ones at which the simulation has been performed, and thus accurately and efficiently locate the density of the two coexisting phases—liquid and vapour—and the coexistence value of the chemical potential.

Below the critical temperature, the vapour and the liquid phase are separated by a large free energy barrier, and the system would not explore both phases during a single simulation run. In order to overcome the free energy barrier in the simulations and to encourage the system to ‘tunnel’ between the two phases we add a term  $k_B T \ln W(\phi)$  to the original Hamiltonian [19]. Choosing the reweighting function  $W(\phi) \approx P(\phi)$  the system samples all densities with roughly the same probability. A good estimate of the reweighting function is provided by histogram analysis [18] of the results at higher temperatures, though other extrapolation schemes can be envisaged [20, 21].

For systems with periodic boundary conditions in all three directions the typical configurations at intermediate average densities consist of a slab of liquid which is separated by two interfaces of area  $L \times L$  from the vapour. The probability of these configurations is suppressed due to the free energy costs of the two interfaces [22]. An example for the free energy  $F(\phi) = -k_B T \ln P(\phi)$  is presented in figure 2(a). The plateau in the free energy (between the minima) indicates that the two interfaces change their mutual distance (and thereby alter the average density) without free energy cost. Therefore they do not interact and the excess free energy is indeed the sum of the individual interface contributions  $2\gamma_{LV}L^2$ . Obviously, an elongated system geometry is advantageous in order to reduce the interaction between the two interfaces. As may be seen, with this methodology a single simulation yields the coexistence value of the chemical potential, the coexistence densities of the liquid and the vapour and the interfacial tension.

While the grand canonical simulations yield already an accurate estimate for the interface tension, we perform simulations in the canonical ensemble at  $T = 1.68$  using a  $18\sigma \times 18\sigma \times 36\sigma$  geometry with periodic boundary conditions in all directions to investigate the local structure at the interface or surface in more detail. Choosing an appropriate number of particles, we can stabilize two liquid–vapour interfaces a distance  $18\sigma \approx 5R_e$  apart.

In principle, one can also measure the interface free energy by monitoring the anisotropy of the pressure tensor across the interface [23]. Close to liquid–vapour coexistence the pressure is very small, but in our model this small value stems from a cancellation of a large positive contribution due to the LJ interactions and a large negative contribution due to the bonding interactions. Accurate measurement of the interface or surface tension via the pressure tensor would require extremely good statistics [24]. For our parameters the error from the analysis of the anisotropy of the pressure tensor is at least one order of magnitude larger than from the reweighting method discussed above (using a comparable computational effort). As the error results from a cancellation of rather noisy data it might not be proportional to the value of the tension (but rather to the value of the virial of the LJ or FENE forces), and the method might become more useful when the tension is larger [23].

In the MC simulations the local interface position fluctuates [25–27]. These capillary waves broaden the apparent profiles in the simulations and experiments, and the measured profiles depend on the lateral length scale on which they are observed. This effect makes a quantitative comparison of interface profiles between the MC simulations and the SCF calculations rather delicate [26, 27]. Analysing the spectrum of the interface fluctuations, however, provides an accurate alternative for measuring the interface tension. Interface fluctuations increase the interface area and for large wavelength they are describable by the capillary wave Hamiltonian [28]. Let  $u(x, y)$  be the local interface position; then the Hamiltonian for the deviations of the local position is given by

$$\mathcal{H} = \int dx dy \left\{ \frac{\gamma_{LV}}{2} (\nabla_{\parallel} u)^2 + \frac{\kappa_{LV}}{2} (\Delta_{\parallel} u)^2 + \dots \right\} \quad (19)$$

(cf also equation (10)). In our simulations, we define a local  $y$  averaged interfacial position  $u(x)$  by minimizing [25, 29]

$$\left| \int_{x-0.25\sigma}^{x+0.25\sigma} dx' \int_0^D dy' \int_{u(x)-3.6\sigma}^{u(x)+3.6\sigma} dz' \left( \phi(x', y', z') - \frac{\phi_{\text{coex}}^L}{2} \right) \right|. \quad (20)$$

This coarse-grained quantity describes the shape fluctuations of the interface and is rather insensitive to local bulk-like density fluctuations. The interface position is Fourier decomposed according to

$$u(x) \sim \frac{a_0}{2} + \sum_k [a(q_k) \cos(q_k x) + b(q_k) \sin(q_k x)] \quad (21)$$

with wavevectors  $q_k = 2\pi k/L$ . With this coarse-grained  $u(x)$  in the capillary wave Hamiltonian, the equipartition theorem yields for the Fourier components  $a(q)$  and  $b(q)$

$$\gamma_{LV}(q) = \frac{2k_B T}{L^2 q^2 \langle a^2(q) \rangle} = \frac{2k_B T}{L^2 q^2 \langle b^2(q) \rangle} \equiv \gamma_{LV} + \kappa_{LV} q^2 + \dots \quad (22)$$

In principle, the value of the interfacial tension so determined also depends on the wavevector  $q$  and we obtain the macroscopic interfacial tension  $\gamma_{LV} = \gamma_{LV}(q \rightarrow 0)$  in the limit of small wavevectors. The results of the MC simulations are presented in figure 3(a). Indeed, the MC data agree with the value of the interfacial tension determined with the reweighting method in the limit  $q \rightarrow 0$ . However, we find a pronounced reduction of the effective interfacial tension at larger  $q$  vectors, which corresponds to a negative bending rigidity  $\kappa_{LV} < 0$  of the interface. A similar analysis of another coarse-grained polymer model has corroborated our finding [30, 31]. Similar deviations have been predicted by Mecke and Dietrich [33] and by Romero-Rochin and Percus [34] in density functional calculations for a LJ monomer fluid. The dependence of the tension on the wavevector  $q$  has also been observed experimentally [32]. Both density functional calculations [33] and experiments [32] observe an increase of  $\gamma_{LV}(q)$  for large wavevectors.

Capillary waves are also detectable in the total scattering function for wavevectors  $\mathbf{q}$  parallel to the interface [35]. For a system with two independent interfaces the increase  $\Delta G = G - G_{\text{bulk}}$  of the scattering due to capillary waves takes the form

$$\begin{aligned} \Delta G(\mathbf{q}_{\parallel}) &\equiv \frac{1}{nN} \left\langle \left| \int d^3 \mathbf{r} \hat{\phi}(\mathbf{r}) \exp(i\mathbf{q}\mathbf{r}) \right|^2 \right\rangle \\ &\approx \frac{\Delta\phi}{nN} \left\langle \left| \int d^2 \mathbf{r}_{\parallel} [u_1(\mathbf{r}_{\parallel}) - u_2(\mathbf{r}_{\parallel})] \exp(i\mathbf{q}_{\parallel} \mathbf{r}_{\parallel}) \right|^2 \right\rangle \\ &= 2 \frac{\Delta\phi^2 L^2}{nN} \frac{k_B T}{\gamma_{LV} q^2} \end{aligned} \quad (23)$$

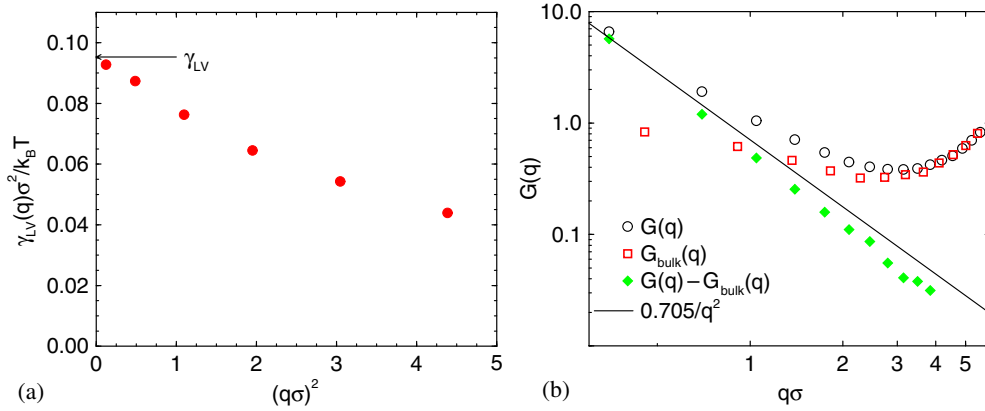


**Figure 3.** (a) Fluctuation spectrum of the local interface position. The arrow marks the value of the interfacial tension obtained from the reweighting method. (b) Global scattering intensity from a system containing two interfaces and the bulk system. The straight line corresponds to capillary waves with the value of the interfacial tension  $\gamma_{LV} = 0.0953$  as measured independently in the simulations (from [24]).

where we have neglected the finite width of the interface.  $u_1$  and  $u_2$  denote the local interfacial positions of the two interfaces and  $\Delta\phi = \phi_{\text{coex}}^L - \phi_{\text{coex}}^V$  is the density difference of the liquid and the vapour [36]. The MC results for the scattering of a system with two interfaces are presented in figure 3(b). The total scattering of the bulk is also shown. For small wavevectors the MC data are well described by the expression above; for finite wavevectors, however, there are deviations. In contrast to the analysis of the interface position, the excess scattering from the interface  $\Delta G(q_{\parallel})$  suggests that fluctuations are suppressed at smaller length scales. We do not expect that interactions among the two interfaces in our system are the major source for the deviations, because these interactions would chiefly modify the fluctuations for small wavevectors. Moreover, identical configurations have been used to analyse the fluctuation of the coarse-grained interface position and the measurement of the scattering. We rather speculate that the decomposition of fluctuations into bulk and interface contributions might be an oversimplification. The interface has a finite (intrinsic) width and we expect the ‘bulk-like’ scattering from the interface region (i.e. scattering of a perfectly planar interface) to differ from the scattering of the coexisting bulk phases.

**3.3.1. Surface properties.** To study profiles of the density and conformational properties at the wall, we use simulations in the canonical ensemble. Except for the vicinity of the drying transition at  $\epsilon_w \approx 0$ , the density rises within a very short distance from the wall to liquid-like values. The presence of an attractive wall strongly suppresses lateral fluctuations of the profile, and the results of the MC simulations can be straightforwardly compared to the results of the SCF calculation.

To measure surface free energies we apply the same grand canonical MC technique in the presence of two walls [24, 37]. The simulations sample all densities between the vapour phase (V) and the liquid phase (L) in contact with the walls. Again the logarithm of the probability distribution yields the free energy as a function of the density. Figure 2(b) displays the results for  $T = 1.68$  at the bulk coexistence value of the chemical potential. The free energy has two minima, corresponding to configurations where either a vapour (low density) or a liquid (high density) phase is in contact with the wall. The ratio of the probability for

finding the system in one of these phases yields the difference in the surface free energies  $2L^2(\gamma_{\text{VW}} - \gamma_{\text{LW}}) = k_B T \ln[P(\phi_L)/P(\phi_V)]$ .

At intermediate densities the typical conformations consist of a liquid slab at each wall. If the system size is large the distance between the liquid–vapour interfaces and the wall and their mutual distance becomes large. In this limit the interfaces neither interact with the walls nor with each other and we expect only a weak dependence of the free energy on the density. Under these conditions one could try to extract an effective interface potential  $g(l)$  for the position of the film away from the wall. The liquid would wet the surface if the plateau value at intermediate densities is lower than the minimum at low densities. However, for the system size studied we do not observe a plateau, i.e. once the interfaces have reached a distance from the wall which is large enough for the effective interaction between the interface and the wall to decay they already begin to interact mutually. Although our simulation cell is not large enough to extract the effective interface potential accurately (because of the presence of two liquid–vapour interfaces in the simulation box) we can reliably determine  $\gamma_{\text{VW}} - \gamma_{\text{LW}}$ . In these limiting states the container is either completely filled with the liquid or the vapour and there are no liquid–vapour interfaces present. The perturbation of the density profile in the liquid extends only over a few  $\sigma$  (cf figure 6), which is much smaller than the extension of the simulation cell.

Once this free energy difference is calculated for a particular strength of the monomer–wall interaction  $\epsilon_w$ , the dependence on the attractive strength of the wall can be obtained via thermodynamic integration:

$$\Omega(\epsilon_w, \mu) = \Omega(\epsilon_0, \mu) + \int_{\epsilon_0}^{\epsilon_w} d\epsilon'_w \frac{\langle E_{\text{wall}}(\epsilon'_w) \rangle}{\epsilon'_w} \quad (24)$$

where  $\Omega$  is the grand canonical potential and  $E_{\text{wall}} = L^2 \int dz \hat{\phi}(z) V_{\text{wall}}(z)$  denotes the interaction energy associated with the monomer–wall interaction potential. However, rather than measuring this wall energy for many different values of the interaction strength  $\epsilon_w$ , we use an expanded ensemble in which the monomer–wall interaction strength  $\epsilon_w$  is a MC variable [24, 37]. This allows us to calculate the free energy difference between different values of the attractive strength  $\epsilon_w$  in a single simulation run. The partition function of the expanded ensemble takes the form

$$\mathcal{Z} \sim \sum_{\{\epsilon_w\}} W_w^{-1}(\epsilon_w) \exp(-\Omega(\epsilon_w)/k_B T) \quad (25)$$

where the reweighting factors  $W_w$  are adjusted so as to achieve uniform sampling of the different  $\epsilon_w$  values. Initial estimates for the reweighting factor have been obtained via equation (24). The MC simulation comprises additionally moves which switch between neighbouring values of the monomer–wall interactions (care has to be exerted at the limiting values to fulfil detailed balance). Let  $P_w(\epsilon_w)$  denote the probability with which the fluctuating wall strength takes the value  $\epsilon_w$ . Then the difference in the surface free energy of the liquid phase is given by

$$\gamma_{\text{LW}}(\epsilon_w) = \gamma_{\text{LW}}(\epsilon_0) - \frac{k_B T}{2L^2} \ln \left( \frac{P_w(\epsilon_w) W_w(\epsilon_w)}{P_w(\epsilon_0) W_w(\epsilon_0)} \right) \quad (26)$$

where the simulations are performed at the coexistence value of the chemical potential and the system is in the liquid phase. If the system is in the vapour phase the expression yields the surface free energy difference of the vapour. This is a computationally efficient method for calculating the dependence of the surface free energy on the attractive strength of the interactions if neither the liquid nor the vapour wets the surface completely. For large attraction  $\epsilon_w$  the liquid wets the surface and the simulation in the vapour phase becomes

metastable (the simulation cell eventually fills with the liquid phase). In the case of a first-order wetting transition, however, the metastable states are well observable in the simulations up to the wetting spinodal. For very small interaction strength the vapour ‘wets’ the wall and the simulation in the liquid phase becomes metastable. At this drying transition the difference  $\gamma_{VW} - \gamma_{LW}$  equals  $-\gamma_{LV}$ . The knowledge of the absolute value of  $\gamma_{VW} - \gamma_{LW}$  at the drying transition can actually be used as an alternative starting value for the thermodynamic integration [38, 39], because the transition shows little metastability (cf section 5).

#### 4. Self-consistent field calculations

##### 4.1. General formalism

In the mean field approximation the problem of many mutually interacting chains in contact with a surface is approximated by that of a single chain in a self-consistently determined field that mimics the effect of interactions with neighbouring molecules. This single-chain problem is then solved using a partial enumeration scheme or resorting to a Gaussian chain model. In this review we use the notation of SCF theories [24, 40] although a completely equivalent description can be obtained using the density functional theory formalism [41–44].

The starting point is the canonical partition function  $\mathcal{Z}$  of  $n$  polymers in a volume  $V$ :

$$\mathcal{Z} \sim \frac{1}{n!} \int \mathcal{D}[\{\mathbf{R}\}] \mathcal{P}[\{\mathbf{R}\}] \exp\left(-\frac{F_{\text{ex}}[\hat{\phi}(\mathbf{r})]}{k_B T}\right) \quad (27)$$

where  $n$  is the number of polymer molecules,  $\mathbf{R}_{i,j}$  denotes the coordinate of the  $j$ th monomer of chain  $i$ ,  $\{\mathbf{R}\}$  is the set of all polymer coordinates and specifies a configuration of polymers,  $\mathcal{D}[\{\mathbf{R}\}]$  denotes a sum over all polymer conformations,  $\mathcal{P}[\{\mathbf{R}\}]$  denotes the probability distribution of chain conformations,  $F_{\text{ex}}$  is the excess free energy functional and  $\hat{\phi}$  denotes the microscopic monomer density generated by the specific polymer configurations, i.e.

$$\hat{\phi}(\mathbf{r}; \{\mathbf{R}\}) = \sum_{i=1}^n \sum_{j=1}^N \delta(\mathbf{r} - \mathbf{R}_{i,j}), \quad (28)$$

where the second sum runs over all  $N$  monomers of a chain.  $\mathcal{P}[\{\mathbf{R}\}]$  is given by

$$\mathcal{P}[\{\mathbf{R}\}] = \mathcal{P}_{\text{melt}}[\{\mathbf{R}\}] \exp\left(-\int d^3\mathbf{r} \frac{V_{\text{wall}}(\mathbf{r})\hat{\phi}(\mathbf{r})}{k_B T}\right), \quad (29)$$

where  $\mathcal{P}_{\text{melt}}[\{\mathbf{R}\}]$  is the probability distribution of chain conformations in the melt (cf below) and  $V_{\text{wall}}(\mathbf{r})$  is the interaction potential between a site and the surface(s). To proceed further, we require an approximation for  $F_{\text{ex}}$ , and some further simplifications as discussed below.

The first simplification we make is to neglect the coupling between the chain conformations and the thermodynamic state of the system<sup>3</sup>. By construction our calculations reproduce the chain conformations characteristic of the concentrated solution which coexists with the vapour phase at temperature  $k_B T/\epsilon = 1.68$ . This is a quite drastic assumption, because the polymer conformations change from a collapsed globule at low polymer concentration to a random walk in the concentrated solution [48]. However, the free energy (of the isolated globule and the liquid) below the  $\Theta$  temperature is chiefly determined by the balance between attractive and repulsive contributions to the monomer–monomer interaction; the conformational entropy appears not to dominate the behaviour. We emphasise, however, that the change of the chain

<sup>3</sup> For spatially homogeneous systems (bulk) the coupling of the chain conformation and temperature, density or composition in blend has been explored in [45–47].

conformations due to a spatial inhomogeneity (wall or liquid–vapour interface) is captured by our calculations (cf figure 3, for instance).

The derivation of a mean field approximation to the partition function equation (27) follows the development of SCF theories of polymers [49–53]. Introducing auxiliary fields  $U$  and  $\Phi$  we rewrite the multi-chain partition function in terms of non-interacting chains:

$$\begin{aligned} \mathcal{Z} &\sim \int \mathcal{D}U \mathcal{D}\Phi \exp\left(-n \ln n + n - \frac{F_{\text{ex}}[\Phi]}{k_B T} + \int d^3\mathbf{r} U(\mathbf{r})\Phi(\mathbf{r}) + n \ln QV\right) \\ &\equiv \int \mathcal{D}U \mathcal{D}\Phi \exp\left(-\frac{\mathcal{F}[U, \Phi]}{k_B T}\right) \end{aligned} \quad (30)$$

where  $V$  is the volume,  $Q[U]$  is the single-chain partition function in the external field  $U$ , i.e.

$$\begin{aligned} Q[U] &= \frac{1}{V} \int \mathcal{D}[\mathbf{R}_1] \mathcal{P}[\mathbf{R}_1] \exp\left(-\int d^3\mathbf{r} U(\mathbf{r})\hat{\phi}(\mathbf{r}; \mathbf{R}_1)\right) \\ &= \frac{1}{V} \int \mathcal{D}[\mathbf{R}_1] \mathcal{P}[\mathbf{R}_1] \exp\left(-\sum_{j=1}^N U(\mathbf{R}_{1,j})\right), \end{aligned} \quad (31)$$

and

$$\frac{\mathcal{F}[U, \Phi]}{Vk_B T} = \frac{\phi_{\text{av}}}{N} \ln \frac{\phi_{\text{av}}}{eN} + \frac{F_{\text{ex}}[\Phi]}{Vk_B T} - \frac{1}{V} \int d^3\mathbf{r} U(\mathbf{r})\Phi(\mathbf{r}) - \frac{\phi_{\text{av}}}{N} \ln Q[U], \quad (32)$$

where  $\phi_{\text{av}} = \frac{nN}{V}$  is the average monomer density.

The functional integral equation (30) cannot be evaluated explicitly and we resort to a saddle point approximation. If fluctuations of the local density are neglected, the values of the field  $U$  and the density  $\Phi$  (denoted by lower case letters) which minimize the free energy functional  $\mathcal{F}$  are given by

$$u(\mathbf{r}) \equiv U_{\text{min}}(\mathbf{r}) = \frac{\mathcal{D}}{\mathcal{D}\Phi} \frac{F_{\text{ex}}[\Phi(\mathbf{r})]}{k_B T} \quad (33)$$

and

$$\begin{aligned} \phi(\mathbf{r}) \equiv \Phi_{\text{min}}(\mathbf{r}) &= -\frac{\phi_{\text{av}} V}{N} \frac{\mathcal{D}}{\mathcal{D}U} \ln Q[U] \\ &= \frac{\phi_{\text{av}} V}{N} \frac{\int \mathcal{D}[\mathbf{R}_1] \mathcal{P}[\mathbf{R}_1] \hat{\phi}(\mathbf{r}, \mathbf{R}_1) \exp(-\int d^3\mathbf{r}' u(\mathbf{r}')\hat{\phi}(\mathbf{r}'; \mathbf{R}_1))}{\int \mathcal{D}[\mathbf{R}_1] \mathcal{P}[\mathbf{R}_1] \exp(-\int d^3\mathbf{r}' u(\mathbf{r}')\hat{\phi}_1(\mathbf{r}'; \mathbf{R}_1))}. \end{aligned} \quad (34)$$

The last expression identifies  $\phi(\mathbf{r})$  as the Boltzmann average of the single-chain density in the external field  $u(\mathbf{r})$ ; it is also the theoretical estimate for the monomer density profile of the polymer fluid. Given an approximation for  $F_{\text{ex}}$  as a function of the density  $\phi(\mathbf{r})$ , equations (33) and (34) form a closed set of self-consistent equations for the fields  $\phi(\mathbf{r})$  and  $u(\mathbf{r})$  from which the density profiles and thermodynamic properties can be obtained. This requires the iterative evaluation of the average in equation (34).

Once the density profile  $\phi(\mathbf{r})$  and the effective field  $u(\mathbf{r})$  which solves the self-consistent equations have been obtained, the free energy is calculated by substituting the solutions in equation (32). All single-chain properties (e.g. segment profiles, orientation) are computed from the Boltzmann average of non-interacting chains in the external field  $u$ .

The numerical procedure is straightforward if computationally intensive. An initial guess for the field  $u(\mathbf{r})$  is first obtained, the monomer density profile is calculated from equation (34) and this procedure is continued until equation (38) is fulfilled. The computationally intensive part is the evaluation of the monomer density profile. The sum ( $\int \mathcal{D}[\mathbf{R}_1] \mathcal{P}[\mathbf{R}_1]$ ) over the single-chain conformations is approximated by a partial enumeration over a large number of

chain conformations [24, 37, 46, 54, 55] extracted from simulations of a homogeneous system at  $k_B T/\epsilon = 1.68$  and coexistence liquid density ( $\phi\sigma^3 = 0.61$ ). Typically  $10^6$ – $10^7$  single-chain conformations are employed for the calculations, and the enumerations are performed in parallel on a CRAY T3E assigning a small fraction of the conformations to each processor. 64 or 128 processors have been employed in parallel and a typical self-consistent calculation of a profile takes a few minutes. The spatial dependence of the field and density profile in equations (31), (34) and (40) is discretized in terms of the real space coordinate perpendicular to the interface/surface.  $D$  denotes the extension of the system in the  $z$  direction perpendicular to the inhomogeneity. Typically, we employ a discretization step of  $\Delta z \approx 0.04\sigma$ . The corresponding set of non-linear equations is solved via a Newton–Raphson scheme.

We use a weighted density approximation (WDA) for the excess free energy functional. Previous density functional calculations [39] and integral equations [56, 57] for LJ *monomeric* fluids close to attractive walls demonstrated that the interface properties may be described in terms of two different interactions. On the one hand, the harsh repulsive interactions, whose range is set by the effective hard core diameter of the monomers, determine the packing of the monomeric units. On the other hand, the attractions, whose range is set by the range of the attractive LJ potential, i.e.  $r_{\max} = 2 \times 2^{1/6}\sigma$ , do not modify the packing to a large degree but may considerably affect the value of the free energy. Since the effects of attraction and repulsion are qualitatively different, an explicit decomposition of the functional into contributions from a harsh repulsion and a weak attraction has proven successful.

We use the same decomposition of the excess free energy functional for our polymer model:

$$\frac{F_{\text{ex}}[\phi(\mathbf{r})]}{k_B T} = \int d^3\mathbf{r} \phi(\mathbf{r}) \{g_{\text{hc}}(\bar{\phi}_{\text{hc}}(\mathbf{r})) + g_{\text{att}}(\bar{\phi}_{\text{att}}(\mathbf{r}))\} \quad (35)$$

where  $g_{\text{hc}}$  and  $g_{\text{att}}$  represent the free energies per monomer due to the repulsive interaction and the attractive interaction, respectively, and  $\bar{\phi}_{\text{hc}}(\mathbf{r})$  and  $\bar{\phi}_{\text{att}}(\mathbf{r})$  are weighted densities, defined by

$$\begin{aligned} \bar{\phi}_{\text{hc}}(\mathbf{r}) &= \int d^3\mathbf{r}' w_{\text{hc}}(\mathbf{r} - \mathbf{r}') \phi(\mathbf{r}') \\ \bar{\phi}_{\text{att}}(\mathbf{r}) &= \int d^3\mathbf{r}' w_{\text{att}}(\mathbf{r} - \mathbf{r}') \phi(\mathbf{r}') \end{aligned} \quad (36)$$

and  $w_{\text{hc}}(\mathbf{r})$  and  $w_{\text{att}}(\mathbf{r})$  are (as yet undetermined) weighting functions that satisfy the normalization condition:

$$\int d^3\mathbf{r} w_{\text{hc}}(\mathbf{r}) = \int d^3\mathbf{r} w_{\text{att}}(\mathbf{r}) = 1. \quad (37)$$

Phenomenologically, the weighting functions  $w_{\text{hc}}$  and  $w_{\text{att}}$  parametrize the spatial extent of the monomer–monomer interactions. The theory is specified by the two thermodynamic functions of state  $g_{\text{hc}}$  and  $g_{\text{att}}$ , and the two weighting functions  $w_{\text{hc}}(\mathbf{r})$  and  $w_{\text{att}}(\mathbf{r})$ . Approximations for these four functions are discussed in the next subsection.

Note that, within the WDA, we can obtain a closed form expression for  $u(\mathbf{r})$ :

$$\begin{aligned} u(\mathbf{r}) &= g_{\text{hc}}(\bar{\phi}_{\text{hc}}(\mathbf{r})) + \int d^3\mathbf{r}' w_{\text{hc}}(\mathbf{r} - \mathbf{r}') \phi(\mathbf{r}') \frac{dg_{\text{hc}}}{d\bar{\phi}_{\text{hc}}}(\mathbf{r}') \\ &\quad + g_{\text{att}}(\bar{\phi}_{\text{att}}(\mathbf{r})) + \int d^3\mathbf{r}' w_{\text{att}}(\mathbf{r} - \mathbf{r}') \phi(\mathbf{r}') \frac{dg_{\text{att}}}{d\bar{\phi}_{\text{att}}}(\mathbf{r}'). \end{aligned} \quad (38)$$

Since we consider only one-dimensional profiles we replace integrals of the form  $\int d^3\mathbf{r} w(\mathbf{r}) \phi(\mathbf{r})$  by  $\int dz w_z(z) \phi(z)$  with

$$w_z(z) = 2\pi \int_0^\infty d\rho \rho w(\sqrt{z^2 + \rho^2}). \quad (39)$$

To obtain the free energy  $F$  we substitute the saddle point values of the field  $w$  and the density  $\phi$  into equation (32), with  $F = \mathcal{F}[\phi, u]$ , which gives

$$\begin{aligned} \frac{F}{Vk_B T} &= \frac{\phi_{\text{av}}}{N} \ln \frac{\phi_{\text{av}}}{N} - \frac{\phi_{\text{av}}}{N} \ln \mathcal{Q}[u] - \frac{1}{V} \int d^3 r d^3 r' w_{\text{hc}}(\mathbf{r} - \mathbf{r}') \frac{dg_{\text{hc}}}{d\phi_{\text{hc}}} \phi(\mathbf{r}) \phi(\mathbf{r}') \\ &\quad - \frac{1}{V} \int d^3 r d^3 r' w_{\text{att}}(\mathbf{r} - \mathbf{r}') \frac{dg_{\text{att}}}{d\phi_{\text{att}}} \phi(\mathbf{r}) \phi(\mathbf{r}'). \end{aligned} \quad (40)$$

The chemical potential,  $\mu$ , takes the form

$$\frac{\mu}{k_B T} \equiv \frac{1}{k_B T} \frac{\mathcal{D}F[\phi, u[\phi]]}{\mathcal{D}\phi(\mathbf{r})} = \frac{1}{N} \ln \frac{\phi_{\text{av}}}{N} - \frac{1}{N} \ln \mathcal{Q}[u[\phi]], \quad (41)$$

and the grand canonical ensemble free energy,  $\Omega$ , is given by

$$\frac{\Omega}{Vk_B T} \equiv \frac{F}{Vk_B T} - \frac{\mu\phi_{\text{av}}}{k_B T} = -\frac{\phi_{\text{av}}}{N} + \frac{F_{\text{ex}}[\phi]}{Vk_B T} - \frac{1}{V} \int d^3 r u(\mathbf{r}) \phi(\mathbf{r}). \quad (42)$$

## 4.2. Choice of the free energy densities and weighting functions

**4.2.1. Thermodynamic properties of the homogeneous system.** As input into the theory, we require the thermodynamic properties of the homogeneous fluid. Since we divide the free energy functional into contributions from the repulsive and attractive parts, we require estimates for the two free energy densities,  $g_{\text{hc}}(\phi)$  and  $g_{\text{att}}(\phi)$ . The total free energy density of the homogeneous fluid is  $g(\phi) \equiv g_{\text{hc}}(\phi) + g_{\text{att}}(\phi)$ . First we consider the total free energy density  $g$  and subsequently the free energy density due to repulsive interactions. The attractive contribution to the free energy density is obtained from  $g_{\text{att}} = g_{\text{TPT1}} - g_{\text{hc}}$ .

We use Wertheim's thermodynamic perturbation theory (TPT1) [58–63] to calculate the total free energy density  $g(\phi)$ . We briefly summarize the salient features; details regarding the implementation of the TPT1 theory to this model are given in [12]. Using the monomer fluid of LJ particles as a reference system, we determine the total free energy of the polymer solution by calculating the effect of the bonding potential  $V_{\text{FENE}}$  as a thermodynamic perturbation. The free energy difference between the polymer solution and the monomeric reference system (LJ) is given by

$$\begin{aligned} \frac{F - F_{\text{LJ}}}{k_B T} &= -\ln \frac{\frac{1}{(n)!} \int \mathcal{D}[\mathbf{r}] \exp\left(-\frac{E_{\text{LJ}}[\mathbf{r}] + E_{\text{FENE}}[\mathbf{r}]}{k_B T}\right)}{\frac{1}{(nN)!} \int \mathcal{D}[\mathbf{r}] \exp\left(-\frac{E_{\text{LJ}}[\mathbf{r}]}{k_B T}\right)} \\ &= -\ln \frac{(nN)!}{n!} - \ln \left\langle \exp\left(-\frac{E_{\text{FENE}}[\mathbf{r}]}{k_B T}\right) \right\rangle_{\text{LJ}} \end{aligned} \quad (43)$$

where  $E_{\text{LJ}}[\mathbf{r}]$  denotes the sum over all LJ interactions and  $E_{\text{FENE}}[\mathbf{r}]$  represents the sum over the  $n(N-1)$  bonding potentials. To first order the last term can be approximated in the form (TPT1) [58–62]:

$$\left\langle \exp\left(-\frac{E_{\text{FENE}}[\mathbf{r}]}{k_B T}\right) \right\rangle_{\text{LJ}} \approx \left[ \frac{1}{V} \int d^3 r_{12} g_{\text{LJ}}(\mathbf{r}_{12}) \exp\left(-\frac{V_{\text{FENE}}(\mathbf{r}_{12})}{k_B T}\right) \right]^{n(N-1)} \equiv \left[ \frac{\delta}{V} \right]^{n(N-1)} \quad (44)$$

where  $g_{\text{LJ}}(\mathbf{r}_{12})$  denotes the pair correlation function of the LJ monomeric reference fluid. This approximation yields the following relation between the free energy density of the LJ monomer fluid and the polymer solution:

$$\frac{F}{Vk_B T} = \frac{\phi}{N} \ln \frac{\phi}{N} + \frac{F_{\text{LJ}}}{Vk_B T} - \phi \ln \phi - \phi \left(1 - \frac{1}{N}\right) \ln \delta \equiv \frac{\phi}{N} \ln \frac{\phi}{N} + \phi g(\phi). \quad (45)$$

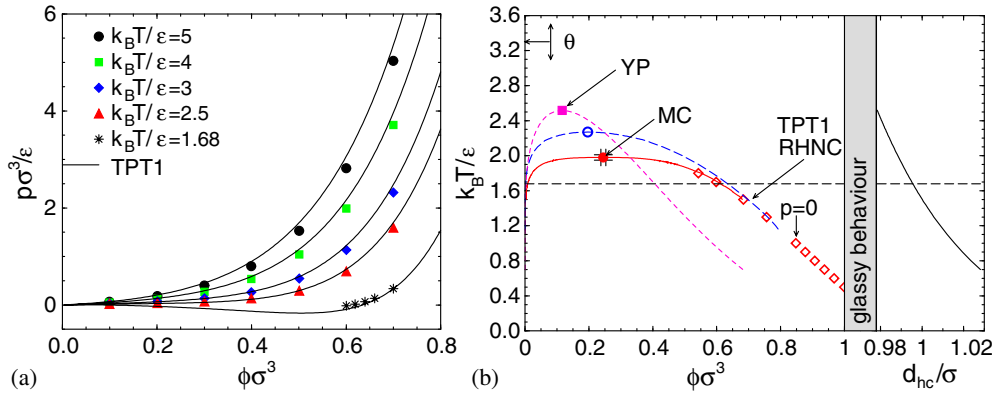


**Figure 4.** (a) Pressure  $p$  as a function of monomer density  $\phi$  for chains of  $N = 10$  monomers. All quantities are measured in LJ reduced units. Symbols are NVT simulation data while lines are predictions from the TPT1 using the RHNC closure for the monomeric reference fluid. From top to bottom, pressure isotherms at  $k_B T/\epsilon = 5, 4, 3, 2.5$  and  $1.68$  (from [12]). (b) Phase diagram of the LJ model for chain length  $N = 10$ . The full curve corresponds to MC results and shows Ising behaviour at the CP. The prediction of TPT1 [12] is shown as a long-broken curve. The critical temperature is higher and the binodals are parabolic in the vicinity of the CP. At lower temperature both calculations agree quantitatively. The dotted curve (YP) corresponds to the van der Waals approximation. Diamonds mark the density in the simulation at which the pressure vanishes. The broken horizontal line marks the temperature  $k_B T/\epsilon = 1.68$  at which we compare numerical theories to MC simulations. The right panel shows the temperature dependence of the hard core diameter (from [70]).

In principle, we could determine the pair correlation function in a separate MC simulation of the monomer fluid. However, the SCF calculations require the knowledge of the  $g_{LJ}$  for many different densities and temperatures. Moreover, the bonded distance is smaller than the typical distance between LJ particles such that we would have to generate very accurate data for  $g_{LJ}$  at small interparticle distances for the evaluation of the above integral. We rather determined the structure and the thermodynamics of the reference system from an integral equation approach. Two closures to the Ornstein–Zernike equations of the reference system have been considered: the mean spherical approximation (MSA) and the reference hypernetted chain (RHNC). Both closures were found to give similar results [12].

The applicability of TPT1 is mainly limited by two conditions:

- Being a mean field theory, TPT1 does not properly account for density fluctuations and overestimates the critical temperature of the polymer fluid.
- The perturbative treatment of the effect of the bonding potential is poor if the structure of the LJ reference fluid differs strongly from the structure of the polymer solution.

In the concentrated regime the fluid structure is determined by the density and is only weakly perturbed by the bonding potential. Hence, TPT1 gives a good description of the melt. Close to the CP of the reference fluid ( $T_c(N=1) \approx 1$ ) and at low densities the structure of the monomer and polymer fluids differs more strongly, so that the agreement is less satisfactory. Additionally, TPT1 neither predicts the density dependence of the polymer structure nor does it properly distinguish between inter- and intramolecular interactions.

In spite of these caveats, TPT1 yields for our model a good description of the binodals (not too close to the CP) and the equation of state without any adjustable parameter. Most important, it provides the free energy also for the unstable homogeneous state inside the miscibility gap without any *ad hoc* extrapolation procedure. The results of TPT1 for the

equation of state (a) and the phase diagram (b) are compared to MC results for chain length  $N = 10$  in figure 4. Good quantitative agreement between TPT1 and MC is achieved without any adjustable parameter. Also the scaling of the CP parameters with chain length has been investigated [12]. TPT1 agrees with the scaling predictions of the Flory–Huggins model in the long chain length limit [64] and captures qualitatively some of the deviations observed in simulations of short chains. Moreover this approach can be generalized to mixtures [65].

The same TPT1 scheme can also be used to obtain the free energy of the repulsive interaction  $g_{\text{hc}}(\phi)$ , which we approximate by those of a system of tangent hard-sphere chains of diameter  $d_{\text{hc}}$ . We obtain the hard core diameter  $d_{\text{hc}}$  using the Barker–Henderson [66] recipe, i.e.

$$d_{\text{hc}} = \int_0^{r_{\text{min}}} dr [1 - \exp(-V_{\text{WCA}}/k_B T)] \quad (46)$$

where the integration is extended to the minimum  $r_{\text{min}} = 2^{1/6}\sigma$  of the LJ potential and  $V_{\text{WCA}}(r) = V_{\text{LJ}}(r) + V_{\text{LJ}}(r_{\text{min}})$  for  $r < r_{\text{min}}$ . For the hard core contribution, we use the TPT1 due to Wertheim [58] which is known to be quantitatively accurate for the volumetric properties of hard chain fluids [58, 60].

For tangent hard chains equation (45) simplifies to

$$g_{\text{hc}}(\phi) = \frac{F_{\text{ex}}^{\text{hs}}}{k_B T n N} - \left(1 - \frac{1}{N}\right) \ln \delta_{\text{hs}} \quad (47)$$

where  $F_{\text{ex}}^{\text{hs}}/nN$  is the excess free energy per particle of a reference fluid of unconnected hard spheres and  $\delta_{\text{hs}}$  is the contact value of the pair correlation function of the reference fluid. The contact value  $\delta_{\text{hs}}$  can be obtained from the hard sphere pressure using the virial theorem, i.e.  $\delta_{\text{hs}} = \pi d_{\text{hc}}^3/(24\phi)[p/(k_B T \phi) - 1]$ . Using the Carnahan–Starling equation of state [67] for hard spheres we obtain [58]

$$g_{\text{hc}}(\phi) = \frac{4\eta - 3\eta^2}{(1 - \eta)^2} - \left(1 - \frac{1}{N}\right) \ln \frac{1 - \eta/2}{(1 - \eta)^3} \quad (48)$$

where  $\eta = \frac{\pi d_{\text{hc}}^3}{6}\phi$ .

The different contributions to the free energy density are presented in figure 5(a). Over the pertinent range of densities, the attractive contribution resembles a linear function of density. This behaviour is expected from a van der Waals theory and shows that the decomposition into repulsive and attractive contributions does not lead to any artefacts. In our numerical calculations we expand the free energy per particle in a fifth-order polynomial in the density.

**4.2.2. Choice of weighting functions.** The other ingredient in the theory is the choice of weighting functions. In previous work on hard chains [68] and LJ chains [24], it has been shown that the theoretical predictions are rather insensitive to the choice of weighting functions. This suggests that some very simple choices for the weighting functions might be adequate. Some guidance in the choice of weighting functions can be obtained from the relation between the second functional derivative of  $F_{\text{ex}}$  with respect to  $\phi(\mathbf{r})$  and the direct correlation function:

$$\left(\frac{\delta^2 F_{\text{ex}}}{\delta\phi(\mathbf{r})\delta\phi(\mathbf{r}')}\right)_{\phi(\mathbf{r})=\phi(\mathbf{r}')=\phi} = -k_B T c(|\mathbf{r} - \mathbf{r}'|) \quad (49)$$

where  $c(|\mathbf{r} - \mathbf{r}'|)$  is the direct correlation function of the homogeneous fluid.

Our first choice, which we will refer to as approximation (1), is to separate the direct correlation function into two contributions, i.e.  $c(r) = c_0(r) + c_{\text{att}}(r)$ , where the first term is due to repulsive interactions and the second is due to attractions. In the low density limit

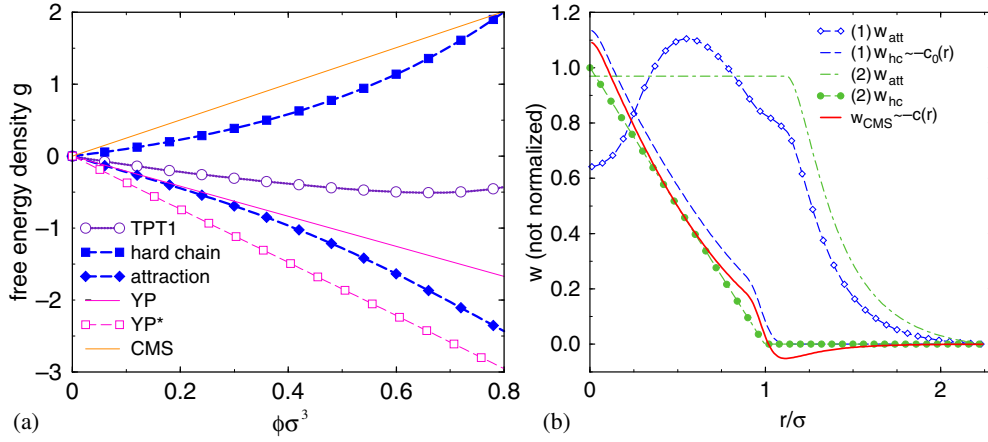


**Figure 5.** (a) Free energy densities as a function of the monomer number density  $\phi$  at temperature  $k_B T/\epsilon = 1.68$ . TPT1 corresponds to Wertheim's perturbation theory for the LJ chains. The results for hard tangent chains are shown as a curve with filled squares. The attractive part of the free energy density is depicted as a broken curve with diamonds. The TPT1 curve (circles) is equal to the attractive part (diamonds) plus the hard chain contribution (filled squares). The full curve with negative slope shows the free energy density of the attraction within the van der Waals approximation (YP). The broken curve with open squares corresponds to the attractive free energy which has been adjusted to give the correct liquid coexistence density (YP\*). The straight full line with positive slope corresponds to the PRISM equation of state used in the calculations (CMS). (b) Unnormalized weighting functions and comparison to the direct correlation function of the full system  $c(r)$  and the tangent hard chain system  $c_0(r)$  as obtained from PRISM theory (from [70]).

$w(r) \sim c(r)$  and we can identify  $w_{\text{hc}}(r) \sim c_0(r)$  and  $w_{\text{att}}(r) \sim c_{\text{att}}(r)$  [70]. The polymer reference interaction site model (PRISM) [69] theory is used to calculate the direct correlation functions [70]. The theory requires, as input, the single-chain structure factor for the chain fluid, which one obtains using the semi-flexible chain model with the semi-flexibility adjusted so that the chain size is the same as in the simulations. The PRISM equations are solved with the Percus–Yevick closure [70]. The full interaction is employed to calculate  $c(r)$  and only the repulsive interaction potential to calculate  $c_0(r)$ .

A much simpler ansatz is to ignore the fluid–fluid correlations altogether and assume the weighting function merely has the same range as the interaction potential. Our second choice, which we refer to as approximation (2), considers the following approximation:

$$w_{\text{att}}(\mathbf{r}) \sim \begin{cases} V_{\text{LJ}}(r_{\min}) & \text{for } r < r_{\min} \equiv 2^{1/6}\sigma \\ V_{\text{LJ}}(r) & \text{for } r_{\min} < r \end{cases} \quad (50)$$

$$w_{\text{hc}}(\mathbf{r}) \sim (1 - |\mathbf{r}|/d_{\text{hc}})\Theta(d_{\text{hc}} - |\mathbf{r}|) \quad (51)$$

where  $\Theta$  is the Heavyside step function, and the weighting functions are normalized as before. The simple form reproduces the qualitative features of the PRISM results for the direct correlation function.

Figure 5(b) depicts the weighting function from these two approximations. In both approximations,  $w_{\text{hc}}(r)$  is a roughly linear function of  $r$  for distances less than the hard core diameter and almost zero for larger distances. On the other hand,  $w_{\text{att}}(r)$  is roughly constant for distances less than the hard core diameter and proportional to the interaction potential for larger distances. These results are quite similar to what is seen in density functional theories of simple liquids. Interestingly, the simple ansatz is qualitatively similar to what is obtained from the PRISM direct correlation functions.

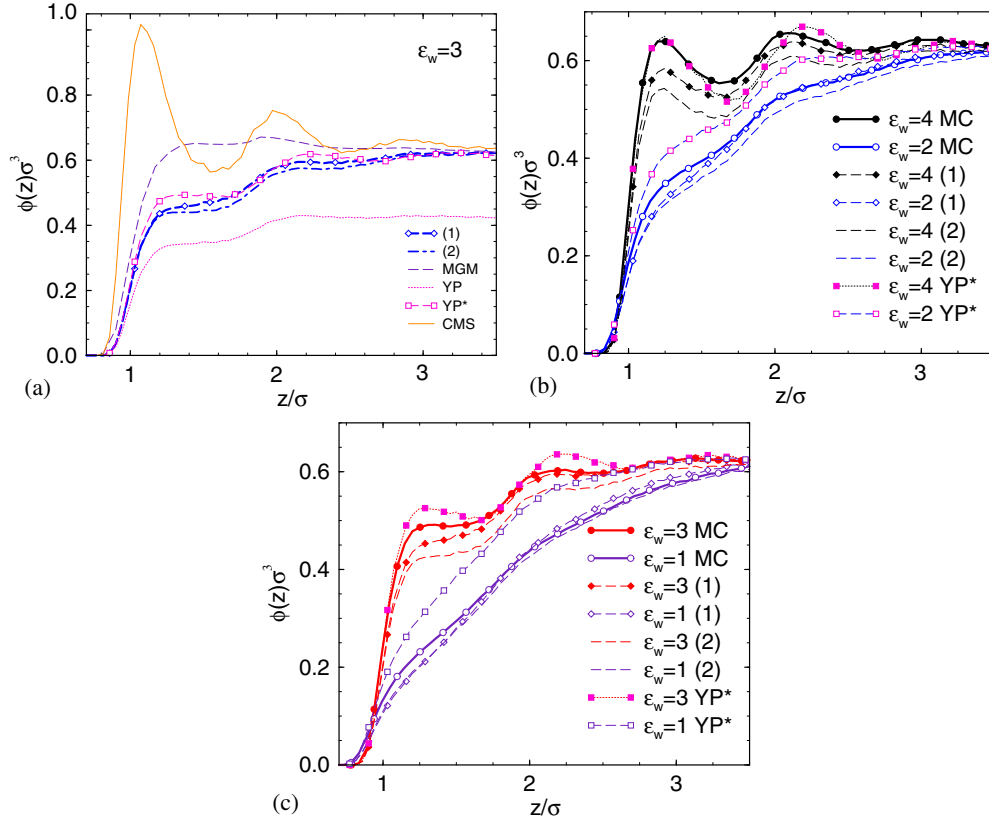


**Figure 6.** (a) Monomer number density profile at an attractive wall  $\epsilon_w = 3$  at temperature  $k_B T/\epsilon = 1.68$ . Monomer number density profile as a function of the attraction  $\epsilon_w$  between the monomers and the wall. (b)  $\epsilon_w = 4$  and 2, (c)  $\epsilon_w = 3$  and 1. Thick curves with circles correspond to MC results, broken curves with diamonds show the results of weighting functions (1), broken curves present the results obtained with weighting functions (2) and dotted curves with squares denote the result of the adjusted van der Waals approximation (YP\*). From [70].

**Table 1.** Free energy densities per particles and weighting functions for the different theories.

	$g_{\text{att}}$	$w_{\text{att}}$	$g_{\text{hc}}$	$w_{\text{hc}}$
(1)	$g_{\text{TPT1}} - g_{\text{hc}}$	$\sim c - c_0$	$g_{\text{hc}}$	$\sim c_0$
(2)	$g_{\text{TPT1}} - g_{\text{hc}}$	$\sim \begin{cases} V_{\text{LJ}}(r_{\text{min}}) & \text{for } r < r_{\text{min}} \equiv 2^{1/6}\sigma \\ V_{\text{LJ}}(r) & \text{for } r_{\text{min}} < r \end{cases}$	$g_{\text{hc}}$	$\sim (1 -  r /d_{\text{hc}})\Theta(d_{\text{hc}} -  r )$
MGM	$g_{\text{TPT1}}$	$\sim \begin{cases} -10(1 -  r /\sigma) & \text{for }  r  < \sigma \\ -\frac{V_{\text{LJ}}(r)}{k_B T} & \text{for }  r  > \sigma \end{cases}$	0	—
YP	$\int d^3 r \min(V_{\text{LJ}}, 0)\phi\sigma^3 / (2k_B T) = -2.49\phi\sigma^3$	$\sim -\min(V_{\text{LJ}}, 0)$	$g_{\text{hc}}$	$\sim \Theta(d_{\text{hc}} -  r )$
YP*	$-3.69\phi\sigma^3$	$\sim -\min(V_{\text{LJ}}, 0)$	$g_{\text{hc}}$	$\sim \Theta(d_{\text{hc}} -  r )$
CMS	$-\int d^3 r c\phi\sigma^3 / (2k_B T) = 2.51\phi\sigma^3$	$\sim c$	0	—

### 4.3. Related theoretical approaches

Our weighted density functional (35) is rather general and alternative numerical theories correspond to specific choices of the free energy densities  $g_{\text{hc}}$  and  $g_{\text{att}}$  and weighting functions  $w_{\text{hc}}$  and  $w_{\text{att}}$ . We will compare these other theoretical approaches to our theory and to MC simulations [24]. The approximations inherent to these other theories are tabulated in table 1 and are described below [70]:

- **MGM.** A simpler theory with a single free energy density and a single weighting function [24] will be used in some applications. This excess free energy corresponds to  $g_{\text{att}} = g_{\text{TPT1}}$  and  $g_{\text{hc}} = 0$ . Even if the weighting function is chosen carefully

$$w(\mathbf{r}) \sim \begin{cases} -10(\sigma - |\mathbf{r}|) & \text{for } |\mathbf{r}| < \sigma \\ -\frac{V_{\text{LJ}}(\mathbf{r})}{k_B T} & \text{for } |\mathbf{r}| > \sigma \end{cases} \quad (52)$$

and, in fact, resembles the direct correlation function obtained from PRISM theory, the predictions for density oscillations in the vicinity of walls will only be in qualitative agreement with MC simulations. In particular, the density in the vicinity of the wall was overestimated and, consequentially, the wetting transition occurred for smaller monomer–wall attractions than observed in the MC simulations [24].

- **YP.** Patra and Yethiraj [43] (YP—to avoid confusion with Percus–Yevick) separated the free energy functional into a repulsive and an attractive contribution with a simple weighting function for the hard sphere contribution and a van der Waals approximation for the attractive contribution. Unfortunately the latter gives a rather poor representation of the equation of state. The phase diagram in the van der Waals approximation is also shown in figure 4(b). The critical temperature is overestimated compared to the MC data or the TPT1, while the liquid density is underestimated at lower temperatures. Only density profiles in the vicinity of a wall were investigated, and the theory became progressively less accurate as the temperature was lowered or the chain length increased. YP argued that this was largely due to the inaccuracies in the van der Waals approximation to the equation of state. In our implementation of this theory, we use a van der Waals approximation for the attractions (YP) and a Heavyside step function for the repulsive weighting function [71].
- **YP\*.** At  $k_B T/\epsilon = 1.68$  the van der Waals approximation underestimates the segregation between liquid and vapour. A better equation of state is obtained by adjusting the attractive free energy density in order to yield the correct density of the liquid at coexistence. The results of the improved equation of state are denoted by YP\*. Unfortunately, the adjustment has to be done at every temperature: in the vicinity of the CP (or at low densities) the van der Waals approximation overestimates the magnitude of the second virial coefficient, while it underestimates its magnitude at low temperatures (or high densities).
- **CMS.** The density functional work by McCoy *et al* [44, 72, 73] also employs a density functional ansatz for the monomer–monomer interactions. It is based on the molecular density functional theory of Chandler, McCoy and Singer (CMS) [74]. Expanding the free energy densities  $g$  around a reference density  $\phi_0$ , i.e.  $g(\phi) = g(\phi_0) + g'(\phi_0)(\phi - \phi_0) + \dots$ , we can cast our equations in the form

$$\frac{F_{\text{ex}}}{k_B T} = \frac{1}{2} \int d^3 r d^3 r' [\phi(\mathbf{r}) - \phi_0] (2g'(\rho_0)w(\mathbf{r} - \mathbf{r}')) [\phi(\mathbf{r}') - \phi_0] + \text{linear terms in } \phi_{\text{av}}. \quad (53)$$

A comparison with the density functional work of McCoy *et al* [44, 72, 73] shows that we obtain their theory when  $g_{hc} = 0$ :

$$w_{\text{att}}(\mathbf{r}) = \frac{c(\mathbf{r})}{\int d^3\mathbf{r} c(\mathbf{r})} \quad (54)$$

and

$$g_{\text{att}}(\phi) = -\frac{\phi}{2k_B T} \int d^3\mathbf{r} c(\mathbf{r}), \quad (55)$$

i.e. this scheme is identical to the previous scheme with a quadratic equation of state and a single weighting function. As the second virial coefficient at  $k_B T/\epsilon = 1.68$  is positive there is no liquid–vapour coexistence and, hence, the equation of state is unsuitable for investigating the wetting behaviour. Nevertheless, the packing of a dense liquid at a wall can be described and the corresponding results are denoted by CMS<sup>4</sup>.

The free energy densities in these different theories are depicted in figure 5(a).

#### 4.4. Comparison between SCF calculations and MC simulations

Figure 6(a) compares the different theoretical predictions for the monomer density profiles of the liquid in contact with an attractive wall for  $k_B T/\epsilon = 1.68$ . Far away from the wall the density is that of the pure liquid. At the surface the density is much lower than the bulk. The value of the density profile increases monotonically from the value at the surface ( $\sim 0$ ) to the bulk value with a sharp increase at  $z/\sigma \sim 1$  and another increase at  $z/\sigma \sim 2$ . In all the theoretical calculations we fix the temperature except for the CMS scheme, where there is no liquid–vapour coexistence and we therefore set  $\phi\sigma^3 = 0.643$  far away from the surface.

Theoretical predictions for the density profiles at a surface are in qualitative agreement with simulations as long as the bulk fluid thermodynamic properties are incorporated accurately. Even though all computational schemes share a similar basis, it is apparent that the density profiles are very sensitive to the free energy density and weighting functions. Of the various theories shown in figure 6(a) some approximations are clearly inadequate. The CMS theory has the correct bulk density (by construction) but the density at the surface is far too high and the oscillations in the density profile are much stronger than seen in simulations. The shape of the density profile predicted by the YP theory is similar to that seen in simulations, but the value of the bulk density is too low. The performance of the MGM theory is superior to the above two theories but the value of the density near the surface is too high compared to the simulations. The approximations (1), (2) and YP\* yield comparable results. These three approaches are in quantitative agreement with the simulations and clearly more accurate than the other approaches.

Panels (b) and (c) of figure 6 compare predictions of approximations (1), (2) and YP\* to MC simulations for a fluid between two walls at a separation  $D = 36\sigma$  and lateral extension  $L = 18\sigma$ . In the canonical simulations we have fixed the average density to  $\phi_{\text{av}}\sigma^3 = 0.577846$ . Various different strengths of the wall–fluid interaction, from  $\epsilon_w = 1$  to 4, are considered. For  $\epsilon_w = 4$  the density of the liquid in the centre roughly corresponds to the liquid density at coexistence. The density profile exhibits oscillations in the vicinity of the wall and reaches the bulk value at around  $z = 1\sigma$ . As  $\epsilon_w$  is decreased, the amplitude of the density oscillations is reduced and a depletion zone gradually builds up in the vicinity of the wall. As the density is reduced at the wall, the density increases in the centre and the chemical potential exceeds

<sup>4</sup> If we would improve the quadratic equation of the state the results would be similar to the scheme (MGM), which uses a weighting function that is very similar to the direct correlation function of the PRISM theory.

the coexistence value  $\mu > \mu_{\text{coex}}$ . At very small monomer–wall interactions there is a drying transition (cf below), i.e. if we were to decrease  $\epsilon_w$  at  $\mu = \mu_{\text{coex}}$  the thickness of the depletion layer would grow macroscopically. At  $\mu > \mu_{\text{coex}}$  the thickness of the depletion layer remains always finite, but it depends sensitively on the chemical potential in the vicinity of the drying transition. A meaningful comparison is only possible if one fixes  $D$  and  $\phi_{\text{av}}$  or the distance  $\mu - \mu_{\text{coex}}$  from the liquid–vapour coexistence.

Approximations (1) and (2) are in quantitative agreement with the simulation data. The period of the density oscillations and their amplitude agrees quantitatively, but for larger values of  $\epsilon_w$  the density is underestimated slightly in the vicinity of the wall. The effect is less pronounced for theory (1), which uses the PRISM direct correlation function, than for (2), which employs a simple approximation for the weighting function.

The YP\* approximation yields the correct density in the vicinity of the wall at large  $\epsilon_w$ , but the amplitude and period of the density oscillations is slightly too large. Similar deviations have been observed for hard chains at hard walls [68] and might be due to the simple form of the weighting function  $w_{\text{hc}}$ . At smaller values of the monomer–wall interaction  $\epsilon_w$  the YP\* calculation systematically underestimates the depletion at the wall. In part this is caused by deviations in the equation of state. Even though the second virial coefficient is chosen to result in the correct liquid density, the compressibility of the liquid is less than that in approximations (1) and (2). If we increase the density in the middle of the film by the same amount, the resulting shift in the chemical potential away from its coexistence value will be larger in the YP\* calculations which, in turn, reduces the thickness of the depletion zone.

Due to the extended shape of the molecules, they orient in the vicinity of the wall, chain ends are enriched and chains' centres of masses are depleted. The conformation characteristics are presented in figure 7. Panel (a) shows the relative density of end segments and centre of masses normalized by the monomer number density. This normalization compensates for the oscillation in the vicinity of the wall and the ratios are rather smooth functions of the distance  $z$  from the wall. There is a pronounced enrichment of chain ends at the wall and a concomitant depletion about  $2.2\sigma$  away from it. Likewise, the centre of masses are depleted at the wall and their density is higher than the average where the chain ends are depleted. Panel (b) shows the orientation of the bond vectors. In the vicinity of the wall bonds orient parallel to the surface. The orientation exhibits small oscillations, i.e. for  $z \approx 1.8\sigma$  the parallel components  $b_x$  and  $b_y$  are slightly smaller than the perpendicular one  $b_z$  and the oscillations die out rapidly at larger distances. The orientation of the largest molecular length scale, the end-to-end vector  $R$ , is presented in panel (c). The  $z$  position of the chain is given by the distance of its centre of mass from the wall. Orientations of the whole chain extend further away from the wall: in the vicinity of the wall the chains are oriented parallel to the wall, at a distance  $z \approx 3.4\sigma$  chains orient slightly perpendicular to the wall. All theories compare very well with the MC data for the conformational properties. The success of the theoretical description of the chain conformations at the wall can be traced back to the enumeration scheme, which takes due account of the chain conformation in the liquid on all length scales. The predictions of approximation (1) are shown in figure 7 and demonstrate quantitative agreement between theory and simulation.

Figure 8 depicts the properties of the liquid–vapour interface at temperature  $k_B T/\epsilon = 1.68$ : panel (a) shows monomer density profiles perpendicular to the interface and panel (b) shows the temperature dependence of the interfacial tension  $\gamma_{\text{LV}}$ . Density profiles from theories (1), (2) and YP\* are all in qualitative agreement, similar to what was seen for a fluid at a surface. The predictions for the interface tension, however, are remarkably different. Panel (b) compares theoretical predictions for the temperature dependence of the interface tension  $\gamma_{\text{LV}}$  to computer simulations. Note that, although approaches (1), (2) and MGM yield an identical

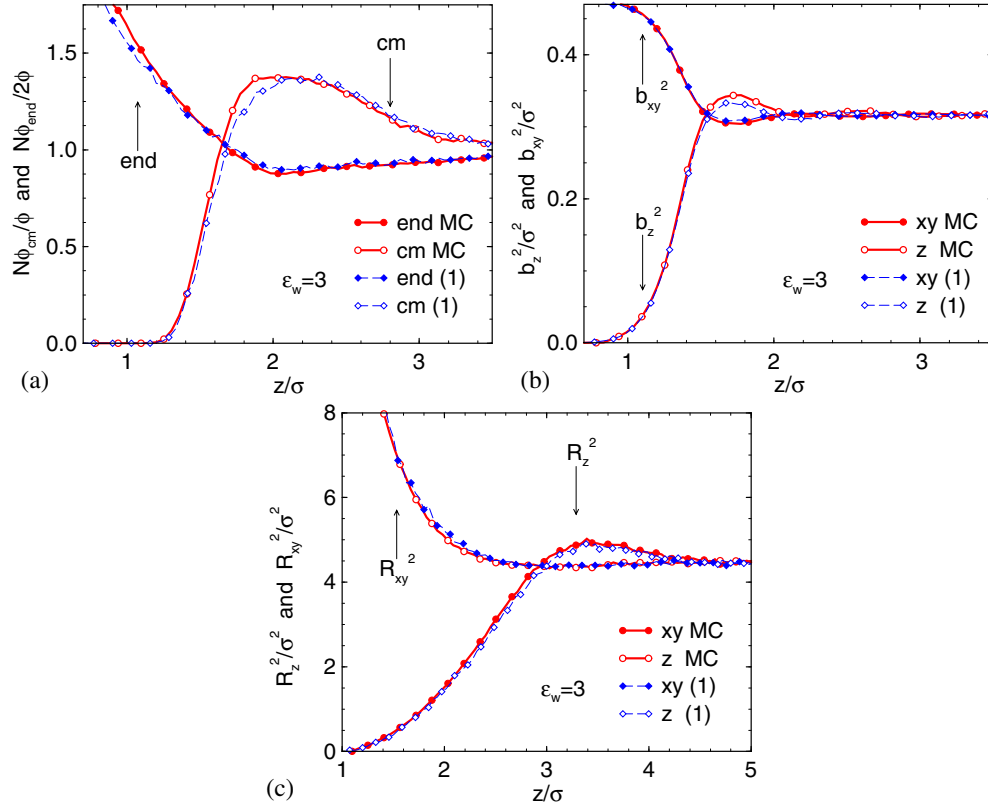


**Figure 7.** (a) Relative density of chain ends and the chains' centres of masses as a function of the distance from the wall at  $k_B T/\epsilon = 1.68$  and  $\epsilon_w = 3$ . (b) Parallel and perpendicular components of the bond vector for the same parameters. (c) Parallel and perpendicular components of the end-to-end vector for the same parameters (from [70]).

bulk phase diagram, they show significant differences for the interface tension. The interface tensions predicted by theories (1) and (2) differ by about 10%, while the theory with a single weighting function (MGM) results in an interface tension which is about a factor 2 lower. Compared to MC data, theories (1) and (2) consistently overestimate the interface tension, which is to be expected from a theory which does not take due account of critical density fluctuations.  $\gamma_{LV}$  vanishes at the critical temperature  $T_c$  which is overestimated by the theory by 15%. At lower temperatures, however, the relative deviations between the MC data and the predictions of (1) and (2) become smaller. The results of the MGM scheme, however, cross the MC data: at high temperatures the interface tension is too large and at lower temperatures it is too small.

The width of the interface is sensitive to the approximations invoked. Since the liquid is far away from the triple point of the LJ monomer fluid, there are no density oscillations on the liquid side of the profile. Using the slope of the profile at the centre, we define the (intrinsic) width of the interface,  $w_{\text{int}}$ , as

$$w_{\text{int}} = \frac{\phi_{\text{coex}}^L - \phi_{\text{coex}}^V}{2(d\phi/dz)} \quad (56)$$

where  $\phi_{\text{coex}}^V$  and  $\phi_{\text{coex}}^L$  are the vapour and liquid coexistence densities, respectively. Similar

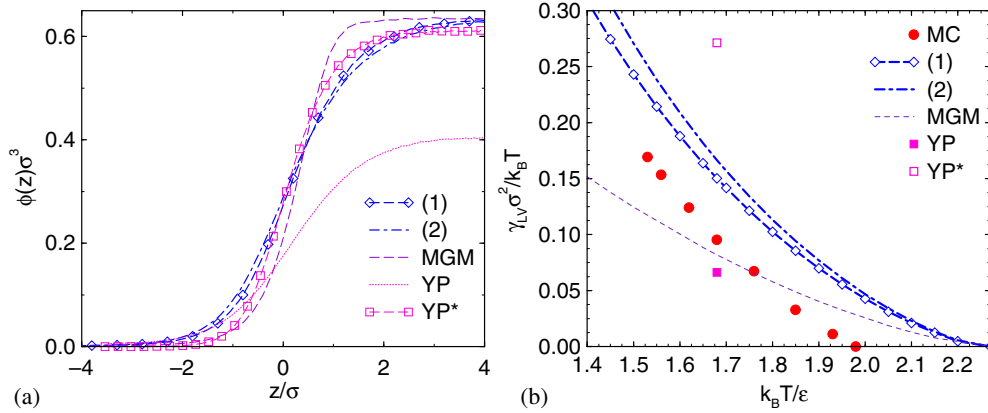


**Figure 8.** (a) Monomer number density profile across the liquid–vapour interface at  $k_B T/\epsilon = 1.68$ . (b) Interface tension as a function of temperature. Circles denote the result of grand canonical MC simulations [24], the broken curve with diamonds depicts the calculations with weighting functions (1), the broken curve corresponds to weighting functions (2) and the thin broken curve shows the result of a single weighting function (MGM) [24]. The results of the van der Waals approximation (YP) and its adjustment YP\* are shown as filled and open squares at temperature  $k_B T/\epsilon = 1.68$ , respectively (from [70]).

**Table 2.** Results of calculations at reduced temperature  $k_B T\epsilon = 1.68$ .

	$\phi_{\text{coex}}^L \sigma^3$	$\phi_{\text{coex}}^V \sigma^3$	$\gamma_{LV}\sigma^2/k_B T$	$w_{\text{int}}/\sigma$	$\Delta\gamma\sigma^2/k_B T^{\text{b}}$	$\epsilon_w^{\text{wet}}$
MC	0.611	0.0083	0.0953	cap. waves	+0.0728	3.22
(1)	0.643	0.0015	0.150	1.20	+0.0723	3.65
(2)	0.643	0.0015	0.166	1.33	+0.0405	4.10
MGM	0.643	0.0015	0.082	0.74	+0.2149	1.98
YP	0.409	0.0026	0.066	1.35	+0.0736	2.90
YP*	0.611	0.0000	0.271	0.89	−0.0305	5.31
CMS	0.643 <sup>a</sup>	—	—	—	−0.6805 <sup>a</sup>	—

<sup>a</sup> CMS: density set by hand, no liquid–vapour equilibrium  $\Delta\gamma \equiv -\gamma_{LV}$ .

<sup>b</sup> at  $\epsilon_w = 3$ .

to the density profiles at an attractive wall, the width of the liquid–vapour interface depends sensitively on the free energy densities and weighting functions. The MGM calculation results in the smallest width, while the YP-scheme yields the largest interfacial width. The data are collected in table 2. We do not attempt to compare the data with MC simulations<sup>5</sup>, because the profiles are broadened in the simulations and experiments, while the theory calculates a hypothetical profile which does not account for fluctuations of the lateral interface position. For the same reason, we also do not discuss profiles of chain conformations across the interface. The previous study [24] showed that good agreement is found on the liquid side of the profile once one accounts for capillary wave broadening. On the vapour side there are, however, deviations because, in the MC simulations, the chains collapse in the bad solvent while there is no conformational change going from the homogeneous liquid to the vapour in the theory. A self-consistent treatment of the chain conformation in a spatially inhomogeneous system is beyond the scope of the present computational scheme.

<sup>5</sup> Profiles through the liquid–vapour interface are shown in figure 14 of [24]. They depend on the lateral system size  $L$ . For  $L = 18\sigma$  we obtain  $w = 2.35\sigma$ .

The values for the liquid–vapour interface tension  $\gamma_{LV}$  are also compiled in the table. The YP calculation yields the lowest interface tension, because the system is much less segregated than in the other calculations. The MGM calculations, which yield the smallest interfacial width, however, give rise to the second smallest interface tension. Theories (1), (2) and YP\* give similar results for the interfacial width, but the YP scheme yields a somewhat lower interface tension. This shows that the width and the interface tension result from a subtle interplay between repulsions and attractions, and details in the choice of the free energy densities are important.

## 5. Wetting on a planar surface

### 5.1. Accurately locating a first-order wetting transition by computer simulations

**5.1.1. Contact angle of droplets.** Several methods have been employed to locate a wetting transition. The most intuitive one is to observe the contact angle of a drop, as is routinely done with great accuracy in experiments. Although in principle the simulation is straightforward [30, 75], some care must be taken. In a grand canonical ensemble, for example, a droplet is unstable and one will rather find the system forming a microscopically thin, homogeneous liquid film below  $T_{\text{wet}}$ , but no drop. In order to observe the droplet as a stable state, it is required to constrain the number of particles to a fixed value. In this case, indeed, a drop can be the thermodynamically stable configuration in a simulation cell of finite size. The situation is similar to that found for spherical droplets [76, 77] at the liquid–vapour coexistence in the bulk.

The chosen box geometry and total number of molecules turns out to be crucial for the droplets to be stabilized. For instance, if the volume to surface ratio of the simulation cell is extremely large, the simulation cell will resemble a grand canonical reservoir, and rather than forming a droplet the particles will distribute homogeneously in the volume. One needs to choose a total surface and number of particles such that spreading of a homogeneous liquid film would result in a film thickness away from the stable region (see figure 1(a)). The behaviour of the excess amount of matter will depend on whether the system is below or above the wetting temperature, however. Below the wetting transition temperature,  $T < T_{\text{wet}}$  a droplet will form whenever the adsorption is above the stable value. The profile of the droplet in the vicinity of the surface will be determined by the interface potential, as discussed previously; only the asymptotic behaviour of a macroscopic drop depends on the minimum of the interface potential. Even in the temperature interval  $T_{\text{wet}} < T < T_{\text{pwc}}$  there are non-stable film thicknesses. They lie between the thickness of the thin and thick adsorption layer of the prewetting coexistence. In this case the vapour condenses onto the surface and increases the thickness of the liquid layer until the volume reaches an undersaturation which corresponds to the chemical potential of the prewetting coexistence  $\Delta\mu_{\text{pw}} < 0$ . On the surface, there will appear thick domains lying on top of a uniform thinner film. The thickness of these two different domains (thin and thick) will be given by the equilibrium values corresponding to the prewetting coexistence (cf figure 1(d)), while their relative amount will be given by the lever rule. The thicker domains may appear as ‘flat’ droplets, but are actually stable thick films above the wetting temperature. The formation of such structures is not in contradiction with Young’s equation. On the contrary, ‘flat’ drops have a finite height and, hence, if one measured the contact angle  $\Theta$  of a (laterally) large ‘flat’ drop, one would obtain  $\Theta = 0$ .

In figure 9 we present radially averaged drop profiles, which have been extracted from simulations at  $k_B T/\epsilon = 1.68$  and various attractive strengths of the surface. The box considered had a size of  $68\sigma \times 68\sigma \times 68\sigma$  and contained 1000 polymer molecules of length  $N = 10$ .

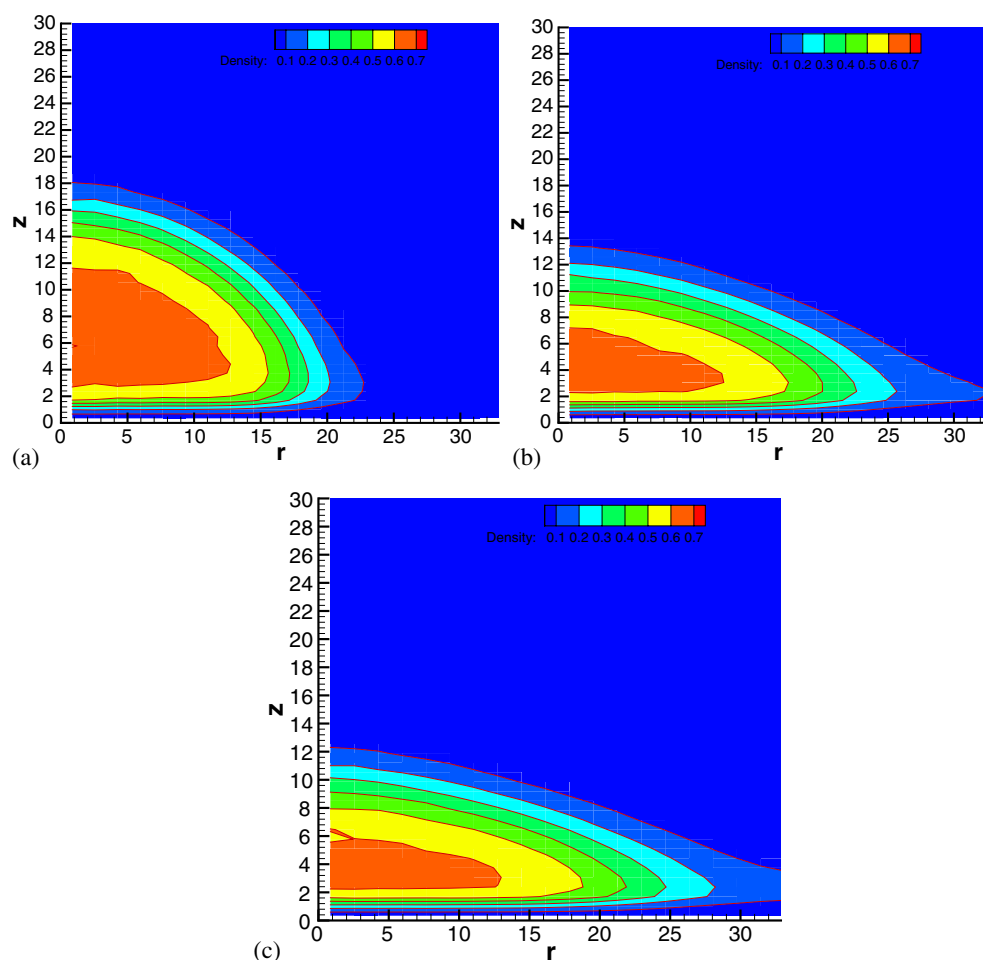


**Figure 9.** Radially averaged density profile of droplets for various strengths of the monomer–wall attraction:  $\epsilon_w = 2.6$  (a) 3.2 (b) and 3.4 (c) (from [75]).

For the weakest attraction  $\epsilon_w = 2.6$  shown in panel (a) a well-defined droplet forms. From the profile we read off an apparent contact angle  $\Theta_{\text{drop}} = 81(4)^\circ$ . This value is comparable with the contact angle of a macroscopic drop as estimated by Young’s equation, which was found to be  $\Theta = 70^\circ$  (see below, cf section 5.1.3). As we increase the value of the attractive strength of the substrate  $\epsilon_w$ , the apparent contact angle decreases gradually. For  $\epsilon_w = 3.2$  we obtain  $\Theta_{\text{drop}} = 52(4)^\circ$  and for  $\epsilon_w = 3.4$  we estimate  $\Theta_{\text{drop}} = 44(4)^\circ$ . Note that, qualitatively, the shape of the small droplet is similar for all three values  $\epsilon_w$ , and from an analysis of the apparent contact angle one would estimate the wetting transition to occur significantly above  $\epsilon_w = 3.4$ . However, the accurate location of the wetting transition is  $\epsilon_{\text{wet}} = 3.22$ , and the contact angle of a macroscopic drop at  $\epsilon_w = 3.2$  is only  $\Theta = 12^\circ$ . The droplet observed for  $\epsilon_w = 3.4$  is therefore a ‘flat’ droplet whose height is dictated by the equilibrium film thickness of the prewetting coexistence.

Unlike the experimental situation which relies on the observation of macroscopic drops, the apparent contact angle of microscopic drops yields only a very inaccurate estimate of the

macroscopic behaviour. In particular, it tends to severely overestimate the contact angle in the vicinity of the wetting transition.

5.1.2. *Measurement of the liquid film thickness in the grand canonical ensemble.* The problems of estimating the wetting transition from the contact angle are two-fold:

- (i) The measurement relies on the observation of a spatial inhomogeneity (drop), and only for very large drops the apparent contact angle agrees with the macroscopic one.
- (ii) The size and geometry of the simulation box matters, because the droplet and the surrounding vapour exchange particles (e.g. the vapour can condense on the surface) so that the system is not exactly at the liquid–vapour coexistence chemical potential.

Both issues can be avoided in the grand canonical ensemble.

One simple approach consists of performing grand canonical simulations at the liquid–vapour coexistence chemical potential, and to monitor the thickness of the liquid film on the surface. Below the wetting transition, we have either  $\epsilon_w < \epsilon_{\text{wet}}$  or  $T < T_{\text{wet}}$ , depending on whether the transition is approached by changing  $\epsilon_w$  or  $T$ , respectively. In this situation, a thin liquid film is stable at the wall. Upon approaching the wetting transition the layer thickness diverges either continuously (at a second-order wetting transition), or discontinuously from a microscopic value to a macroscopic value (in a first-order transition). Above the wetting transition a macroscopically stable film is stable. Thus, starting below the wetting transition with a finite liquid layer one can increase  $\epsilon_w$  or  $T$  and estimate the location of the transition by the divergence of the film thickness. At a first-order wetting transition there are, however, two caveats:

- (i) Even above the wetting transition a thin liquid layer might be metastable and, thus, one rather estimates the location of the wetting spinodal instead of the wetting transition. At a strong first-order wetting transition this might result in a significant overestimation of the location of the wetting transition.
- (ii) If one uses a simulation cell with two symmetric walls, as we do in our simulations, and further sets the chemical potential to its coexistence value, the most stable configuration consists of a simulation cell filled with liquid.

The monitored state made of two liquid films adsorbed on the wall is metastable and requires decreasing the chemical potential below coexistence in order to become stabilized (capillary condensation, cf also figure 2(c)). This metastability of the starting configuration severely limits the length of the simulation runs. Indeed, using such a scheme, we estimate the divergence of the wetting layer for  $k_B T/\epsilon = 1.68$  to be at  $\epsilon_w = 3.4$ . As expected, this value is larger than the accurate location of the wetting transition  $\epsilon_{\text{wet}} = 3.22$ .

Caveat (i) might be overcome by monitoring the probability distribution  $P(l)$  of the layer thickness  $l$ . This gives direct information about the interface potential  $g(l)L^2 = -k_B T \ln P(l)$ , where  $L^2$  denotes the surface area. At a first-order wetting transition the free energy barrier between the thin and the (macroscopically) thick layer might be overcome by reweighting techniques (cf section 3.3 and figure 2(c)).

The second restriction could be alleviated by choosing an attractive and a repulsive wall, thus stabilizing a single liquid–vapour interface in the simulation cell. Ideally, one could choose antisymmetric surface interactions such that the contact angle of a liquid drop on the wall equals the contact angle of a bubble at the opposite wall, and no capillary condensation would occur. While this is a promising route for symmetric mixtures [37, 78] it might be not straightforward if the coexisting phases are not related by symmetry.

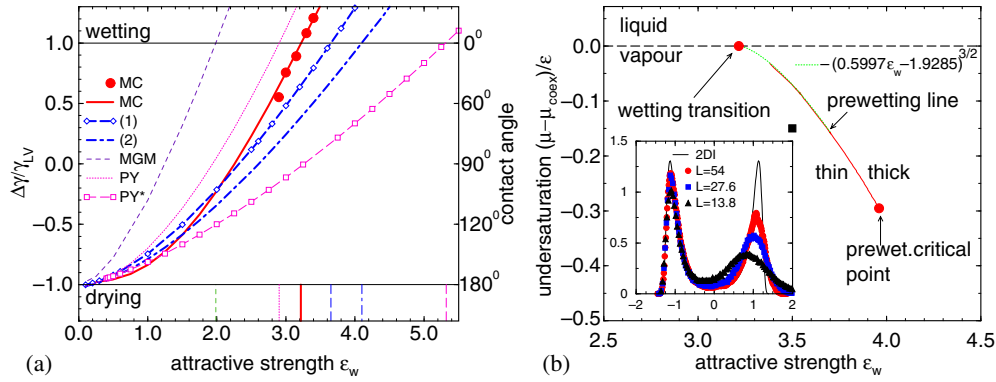


**Figure 10.** (a) Ratio between the difference in the surface tension and the interface tension as a function of the attraction between monomers and wall at  $k_B T/\epsilon = 1.68$ . The location of the wetting transitions is shown at the bottom. Filled circles and the thick full curve represent the MC results. The broken curve with open diamonds corresponds to the calculations with weighting functions (1), the thick chain curve depicts the results with weighting function (2), the thin broken curve is the result of using a single weighting function (MGM), the thin dotted curve shows the scheme (YP) and the thin broken curve with open squares denotes the calculation with the adjusted van der Waals approximation (YP\*) (from [70]). (b) Wetting and prewetting at  $k_B T/\epsilon = 1.68$ . The horizontal broken curve marks the liquid–vapour coexistence, the full curve presents the results for the prewetting curve. In the vicinity of coexistence a fit according to the Clapeyron equation (59) is shown. The wetting transition and the prewetting CP are marked. The filled square marks the simulation point used for patterned substrates in figure 13. The inset displays the probability distribution of the layer thickness normalized to zero mean and unit variance for the system size  $L/\sigma = 13.8, 27.6$  and  $54$  at  $T = 1.68$  and our estimate of the prewetting CP  $\epsilon_w = 3.96$ . At this CP the normalized distribution depends only on the universality class and the corresponding function for the 2D Ising model is also shown (from [24]).

**5.1.3. Young's equation.** By exploiting the ability of the grand canonical ensemble to measure free energy differences, the problems with capillary condensation and metastability may be avoided altogether. In one simulation with standard periodic boundary conditions, one calculates the liquid–vapour interface tension, as described previously. In another set of simulations, one considers a cell made of two parallel walls and periodic boundary conditions in the remaining directions. By monitoring the density fluctuations, one obtains directly the free energies of figure 2(c). The curves show two minima, corresponding to configurations where either the vapour phase or the liquid phase are in contact with the walls. Therefore, the free energy difference between these two states allows us to obtain directly  $\Delta\gamma = \gamma_{VW} - \gamma_{LW}$ . Each of these quantities may be measured in the simulations with a relative accuracy of a few per cent. An additional advantage is that one obtains accurate estimates for rather modest system sizes. Unlike the measurement of the effective interface potential  $g(l)$  one does not regard the free energy of the liquid film bound to the wall and, hence, one needs not to choose the system size large enough such that both the interactions of the liquid–vapour interfaces with the walls and among themselves can be neglected. Having calculated  $\gamma_{LV}$  and  $\gamma_{VW} - \gamma_{LW}$ , one can employ Young's equation (equation (1)) in order to measure the contact angle and the wetting temperature, as shown in figure 10(a). This method yields the accurate estimate  $\epsilon_{\text{wet}} = 3.22$  for the wetting transition at temperature  $k_B T/\epsilon = 1.68$ .

The difference of the surface free energies approaches  $-\gamma_{LV}$  for small values of  $\epsilon_w$  and the vapour dries the wall. The free energy difference approaches the value  $-\gamma_{LV}$  with a very small slope. This indicates that the transition is very weak first order and we cannot rule out a second-order transition. The weakness of the transition explains the lack of metastability

which is observed in the simulations. A very similar behaviour is found for monomeric LJ fluids [38, 79] and a careful study of finite size effects is necessary [79] to accurately pinpoint the location of the drying transition and its order.

*5.1.4. Extrapolating the prewetting line towards coexistence.* If the wetting transition is first order, there will be a concomitant jump in the layer thickness above the wetting temperature away from the coexistence curve in the  $\epsilon_w - \mu$  plane. At this prewetting line, a thin adsorbed layer coexists with a thick layer. In the vicinity of the prewetting line the probability distribution of the layer thickness is bimodal and we can accurately locate the prewetting coexistence by the equal weight rule (cf section 3.3). The prewetting line is presented in figure 10(b).

The prewetting line ends in the prewetting CP. Here, the difference in the layer thicknesses vanishes. This transition is believed to belong to the 2D Ising universality class [80]. Since the correlation length of density fluctuations parallel to the surface diverges at this point, effects of the finite lateral extension of the simulations cell have to be investigated carefully. The normalized probability distribution of the layer thickness at our estimate for the prewetting CP is presented in the inset of figure 10(b). Due to field mixing effects [81] the distribution is asymmetric, but upon increasing the system size we decrease the asymmetry of the distribution. Adjusting the attractive strength of the substrate to map the normalized distribution onto the universal scaling function of the 2D Ising universality class we obtain the estimate  $\epsilon_{\text{pwc}} = 3.96(6)$  for the prewetting CP. This value is also marked in the wetting phase diagram (figure 10(b)).

The approach of the prewetting to the coexistence curve has been studied by Hauge and Schick [82]. The differential of the surface contribution to the thermodynamic potential  $\Omega(\epsilon_w, \mu)$  is given by (cf equation (24))

$$\frac{d\Omega_s}{L^2} = \frac{\langle E_{\text{wall}} \rangle}{\epsilon_w L^2} d\epsilon_w - \Sigma^{\text{ex}} d\Delta\mu \quad (57)$$

where  $\Sigma^{\text{ex}} \approx \Delta\phi l/N$  denotes the polymer excess in the enrichment layer of thickness  $l$  at the surface while  $\langle E_{\text{wall}} \rangle$  denotes the average wall energy felt by the adsorbed film. At the prewetting line a thin  $l_{\text{thin}}$  and a thick layer  $l_{\text{thick}}$  coexist and, hence, their change in  $\Omega_s$  along the prewetting line is the same. This yields the following Clapeyron equation [82]:

$$\left. \frac{d\Delta\mu}{d\epsilon_w} \right|_{\text{prewet}} = \frac{(\langle E_{\text{wall}} \rangle_{\text{thick}} - \langle E_{\text{wall}} \rangle_{\text{thin}})/\epsilon_w L^2}{\Sigma_{\text{thick}}^{\text{ex}} - \Sigma_{\text{thin}}^{\text{ex}}}. \quad (58)$$

Close to the coexistence curve  $l_{\text{thick}}$  is very large. The difference in the surface excess increases to leading order linear in the film thickness,  $\Sigma_{\text{thick}}^{\text{ex}} - \Sigma_{\text{thin}}^{\text{ex}} \approx \Delta\phi l_{\text{thick}}/N$ , while the difference in the wall energies approaches a constant value with growing  $l_{\text{thick}}$ . To a rough approximation this constant takes the value  $-\Delta\phi(9/l_{\text{thin}}^8 - 3/l_{\text{thin}}^2)$ :

$$\left. \frac{d\Delta\mu}{d\epsilon_w} \right|_{\text{prewet}} \approx -\frac{N(9/l_{\text{thin}}^8 - 3/l_{\text{thin}}^2)}{l_{\text{thick}}} \sim -\frac{1}{l_{\text{thick}}} \sim \Delta\mu^{1/3}. \quad (59)$$

Above the wetting transition temperature the layer thickness increases like  $l_{\text{thick}} \sim |\Delta\mu|^{-1/3}$  (complete wetting). Integration of equation (59) yields  $\Delta\mu|_{\text{prewet}} \sim (\epsilon_w - \epsilon_w^{\text{wet}})^{3/2}$  [82]. This dependence can be used to extrapolate the prewetting line towards the coexistence curve and estimate the location of the wetting transition. The approach of the prewetting line in the MC simulations and the SCF calculations is presented in figure 10(b). The extrapolation agrees with the estimate obtained from the Young equation.

### 5.2. Comparison between MC simulations and SCF calculations

To investigate the wetting behaviour of the polymer liquid in the SCF theory we calculate the surface free energy as a difference between the grand canonical potential of the system in the presence of a wall and that of a homogeneous system:

$$\frac{\gamma}{k_B T} \equiv \frac{\Omega - \Omega_{\text{hom}}}{k_B T A} = \frac{(F - \mu\phi_{\text{av}}V + pV)D}{V k_B T} \quad (60)$$

where  $\Omega_{\text{hom}}$  is the grand canonical free energy of a homogeneous system and  $A$  denotes the area of the wall. The contact angle  $\Theta$  of a macroscopic polymer drop on a wall is controlled by the difference between surface tensions,  $\Delta\gamma = \gamma_{WV} - \gamma_{WL}$ , on the one hand, and by the liquid–vapour interface tension,  $\gamma_{LV}$ , according to  $\cos \Theta = \frac{\Delta\gamma}{\gamma_{LV}}$ . The values of the difference of the surface tension  $\Delta\gamma$  at  $k_B T/\epsilon = 1.68$  and  $\epsilon_w = 3$  are compiled in table 2. Again, the different approximation schemes give vastly different values. The best agreement with the MC simulations is obtained by theory (1), while the worst deviations are observed for the CMS scheme.

The dependence of the contact angle on the monomer–wall attraction  $\epsilon_w$  is presented in figure 10(a). Theories (1) and (2) yield good agreement with the MC simulations. Using the direct correlation function from PRISM theory in scheme (1) appears to improve the agreement slightly when compared to scheme (2), which uses a phenomenological ansatz for the weighting functions. The YP theory also gives reasonable values for the contact angle. The agreement is, however, fortuitous, because it underestimates both the interfacial tension and the surface tension substantially and these errors tend to cancel. The MGM and YP\* theories overestimate and underestimate the contact angle, respectively.

Having assessed the accuracy of the SCF approach by comparing it quantitatively to MC simulations, we demonstrate its usefulness by discussing in the following sections some applications of the SCF calculations to slightly more complicated but experimentally relevant situations.

## 6. Interplay between short-range and long-range interactions

Dewetting experiments can probe the subtle features of the interface potential. The minimum of the interface potential is related to the contact angle  $\Theta$  via  $g_{\text{min}} = \gamma(\cos \Theta - 1)$ , and the kinetics of the dewetting process tells a great deal about the curvature of the interface potential: if the curvature is negative, the spinodal dewetting occurs which is characterized by a dominant lateral length scale. If the curvature is positive, the film is locally stable and dewetting (if it occurs) proceeds via nucleation of holes.

A standard experimental system is polystyrene (PS) on a silicon (Si) wafer which is coated by a thin oxide layer of thickness  $d_{\text{ox}}$ . Such a situation is sketched in figure 11(a). Experiments by Müller-Buschbaum *et al* [83] reveal a rather intriguing dewetting behaviour as illustrated in figure 11(a). At high temperature,  $T = 165^\circ\text{C}$ , the polymer dewets and forms drops. These macroscopic drops sit on a mesoscopic film of thickness  $l^* = 22(6) \text{ \AA}$ . Upon cooling below the glass transition temperature  $T_g \approx 100^\circ\text{C}$ , this mesoscopic film between the drops dewets and forms nano-droplets of diameter  $68(8) \text{ nm}$ . As the polymer film becomes glassy, these nano-droplets do not coalesce into macroscopic drops. One observes a dewetting morphology with two distinct drop sizes: macroscopic drops and nano-droplets.

Assuming that the dewetting morphology observed in the experiments is caused by *static* wetting properties, we can rationalize this two-stage dewetting process by an interface potential that exhibits two minima—one corresponds to the mesoscopic film which is stable at high

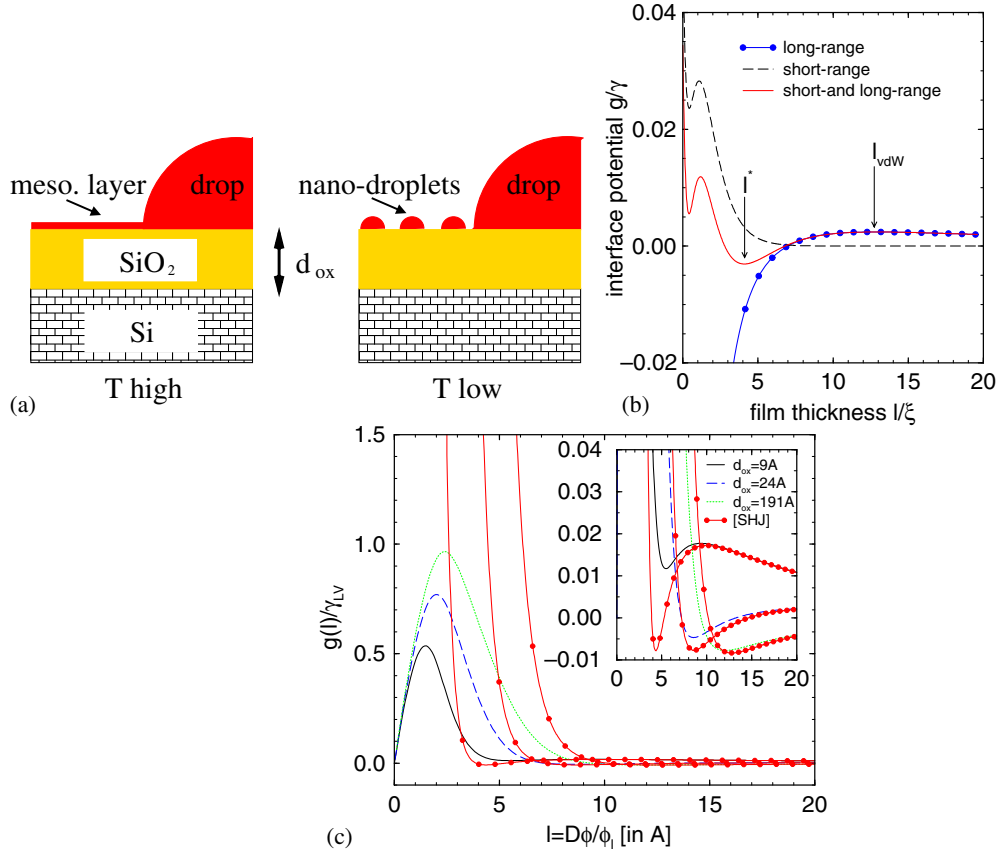


**Figure 11.** (a) Sketch of the polymer film on top of a bilayer substrate, consisting of Si and a thin oxide layer.  $l$  denotes the thickness of the polymer film and  $d_{ox}$  the thickness of the oxide layer. At high temperatures macroscopic drops sit on top of a mesoscopic film. At low temperatures, the mesoscopic film becomes unstable and breaks up into smaller drops. (The relative size of the nano-droplets and the macroscopic drops is not to scale.) (b) Schematic illustration of nano-dewetting. Weak but long-ranged van der Waals interactions determine the interface potential at long distances. They repel the interface at large distances  $l > l_{vdW}$  and attract the interface at intermediate distances. Strong but short-ranged contributions to the interface potential arise from the distortion of the density profile in the vicinity of the substrate. These forces tend to stabilize a microscopically thin film, and they repel the interface at intermediate and large distances. The interplay between van der Waals and short ranged interaction might result in two competing minima. (The relative magnitude of the short- and long-ranged forces is not to scale). (c) Effective interface potential  $g(l)$  for various oxide layer thicknesses. The contact interaction  $V_c$  has been chosen such that the minima at  $l \approx 0$  and  $l \rightarrow \infty$  have almost equal free energy:  $V_c = 3.26\epsilon$  for  $d_{ox} = 9 \text{ \AA}$ ,  $V_c = 1.4\epsilon$  for  $d_{ox} = 24 \text{ \AA}$  and  $V_c = 0.89\epsilon$  for  $d_{ox} = 191 \text{ \AA}$ . The chain curve [SHJ] corresponds to the results of [85]. The inset presents an enlarged view of the minimum at the mesoscopic film thickness (from [86]).

temperatures, and one corresponds to a microscopic, vanishingly small thickness  $l \approx 0$ , which is stable at lower temperatures.

As detailed in the introduction, both short-range and long-range interactions contribute to the interface potential. The length scale of the short-range interaction in equation (4) is of the order of the width  $\xi$  of the interface between the dense polymer melt and its vapour, which is

typically only of the order of a few ångström. Balancing short- and long-range contributions, one finds that the short-range contribution dominates for

$$l \ll l_{\text{cross}} = \xi \ln\left(\frac{\gamma}{g_{\text{lr}}(l_{\text{cross}})}\right). \quad (61)$$

Hence short-range forces are important for extremely thin polymer films or when the Hamaker constant, which controls the strength of the long-range interaction is small. The latter condition is fulfilled, for instance, when the contact angle of the polymer liquid is very small.

The influence of the long-range interactions can be reduced effectively by coating the substrate with a thin oxide layer (Ox). In this case equation (7) has to be replaced by [83, 84]

$$g_{\text{lr}}(l) = \frac{1}{12\pi} \left( -\frac{A_{\text{PSPS}} - A_{\text{PSOx}}}{l^2} + \frac{A_{\text{PSSi}} - A_{\text{PSOx}}}{(l + d_{\text{ox}})^2} \right) \quad (62)$$

where  $A_{\text{PSPS}}$ ,  $A_{\text{PSSi}}$  and  $A_{\text{PSOx}}$  denote the Hamaker constants of the polymer, the polymer and the substrate, and the polymer and the coating layer. Specifically for PS on an oxide-covered Si wafer the Hamaker constant of the oxide coating is smaller than the Hamaker constants of the polymer and the substrate and both terms in the equation above tend to cancel. In this case the long-range part of the interface potential alone exhibits a maximum at a film thicknesses  $l_{\text{vdW}} \sim d_{\text{ox}}$  of a few nanometres. In figure 11(b) we illustrate how the interplay between short- and long-range contribution results in two local minima of the interface potential. The minimum at microscopic film thickness is only due to short-range forces: the corresponding barrier signals the free energy costs of forming a (hypothetical) homogeneous film which is thinner than  $\xi$ . The second minimum at a mesoscopic film thickness  $l^* < l_{\text{vdW}}$  arises from the interplay of both contributions: The short-range part repels the liquid–vapour interface from the substrate, but it decays rapidly as the film thickness grows. The long-range contribution attracts the liquid–vapour interface for thickness  $l < l_{\text{vdW}}$ .

This qualitative explanation relies on two assumptions:

- (i) The phenomenological form of the short-range contribution does neither specify the length scale  $\xi$  of the short-range interaction nor its strength. Additional contributions due to the entropy loss of the polymers due to the confinement in a thin film are neglected.
- (ii) The long-range contributions have to be cut-off at small film thickness  $l$ . If we used the expression for the long-range contribution (62) at small distances  $l \rightarrow 0$  the long-range forces would diverge.

We recall, however, that one obtains the form of the long-range contributions by integrating the interactions between the liquid and the substrate using a sharp-kink approximation for both the liquid–substrate and the liquid–vapour interface (cf equation (6)). For thin films this assumption of a trivial density profile breaks down: in fact, the very distortion of the density profile gives rise to the short-range contribution to the interface potential.

In the following we use SCF calculations, which do not invoke these assumptions, to corroborate the explanation of the experimental finding. Starting from the interactions between the liquid and the substrate we calculate the detailed form of the density profile and the free energy of the liquid film.

To compare the SCF calculations to the experiments we choose the parameters of our computational model to be comparable to the experiments on PS. The LJ chains of  $N$  beads do neither capture details of 8.7k PS on an atomistic scale, nor do we adjust the equation of state of our model to experimental data on the  $pVT$  behaviour of PS. Therefore, we cannot expect agreement between our computational model and experiments on all quantities simultaneously and we identify the model parameters to match quantities pertinent to the wetting behaviour.

We use a chain length  $N = 84$ , which corresponds to the number of repeat units in the experiments. As the number of single-chain conformations increases exponentially with chain length, the partial enumeration scheme would require a very large number of single-chain conformations to capture the orientation and deformation of the chains at the substrate and the liquid–vapour interface. Therefore, we rather use the Gaussian chain model, for which the single-chain partition function can be calculated numerically exactly. The statistical segment length  $b = 1.3\sigma$  is chosen so as to reproduce the chain extension of the bead-spring model. The length scale in the calculations is set by the radius of gyration  $R_g = b\sqrt{N}/\sqrt{6}$ . In the calculations  $R_g \approx 4.8\sigma$  while the experimental value is  $R_g = 25.4 \text{ \AA}$ . Hence, we identify  $\sigma = \sqrt{6}R_g/[b/\sigma]\sqrt{N} = 5.22 \text{ \AA}$ . Not including any architectural details on the segmental length scale, we use a local density functional (i.e.  $w_{\text{hc}}(r) = w_{\text{att}}(r) = \delta(r)$ ) in conjunction with the TPT1 equation of state (employing the MSA closure for the monomer reference fluid). The density of PS at  $T = 413 \text{ K}$  is  $\rho = 1 \text{ g cm}^{-3}$ . This corresponds to  $6.9 \times 10^{-5}$  molecules  $\text{\AA}^{-3}$  or a segment density of  $\phi_l \approx 6.9 \times 10^{-5}(\sqrt{6}R_g/\text{\AA})^3/b^3\sqrt{N} = 0.83\sigma^{-3}$  in LJ units. We adjust the temperature  $k_B T/\epsilon$  such that the density of the liquid (in coexistence with the vapour) matches the experimental density. This yields  $k_B T/\epsilon \approx 0.96$  in LJ units (or  $\epsilon = 0.57 \times 10^{-20} \text{ J}$ ). The critical temperature  $T_c \approx 2.96\epsilon/k_B T$  for chain length  $N = 84$  corresponds to  $1300 \text{ K}$ , which is well beyond the thermal stability limit. For these values of parameters the SCF calculations yield for the interface tension the value  $\gamma = 0.36\epsilon/\sigma^2$ . Using the estimates for  $\sigma$  and  $\epsilon$  we find this value to be about a factor 4 smaller than the experimental data  $\gamma = 0.031 \times 10^{-20} \text{ J \AA}^{-2}$  at  $T = 140^\circ\text{C}$ . If we used a non-local density functional with different weighting functions for attractive and repulsive interactions, the SCF calculation would yield a larger interface tension (cf section 4.4 and figure 7(b)). We emphasise, however, that no experimental input about the  $pVT$  behaviour has been used to parametrize the free energy density and no specific information about the atomistic structure of PS enters the calculation. Consequentially, we consider the SCF result for the interface tension  $\gamma_{\text{LV}}$  rather as an estimate of a typical interface tension of a polymer liquid in coexistence with its vapour than a prediction for the specific system at hand.

The long-range part of the effective interface potential has been extracted from a careful analysis of dewetting experiments. Although the experiments of Seemann *et al* [85] employ shorter chains (2k PS), we do not expect the van der Waals interactions to exhibit a strong dependence on chain length. The experimental data can be parametrized by

$$\frac{g_{\text{exp}}(l)}{\gamma_{\text{LV}}} = A \left( -\frac{1}{l^2} + \frac{r}{(l + d_{\text{ox}})^2} + \frac{c(d_{\text{ox}})}{4l^8} \right) \quad (63)$$

with parameters  $A = (A_{\text{PSPS}} - A_{\text{PSOX}})/12\pi$ ,  $\gamma_{\text{LV}} = 1.88 \text{ \AA}^2$ ,  $r = (A_{\text{PSSI}} - A_{\text{PSOX}})/(A_{\text{PSPS}} - A_{\text{PSOX}}) = 6.9$  and  $c(d_{\text{ox}}) = 3.5 \times 10^5 \text{ \AA}^6$  for an oxide layer of  $d_{\text{ox}} = 24 \text{ \AA}$  [85]. The first two terms represent the long-range interaction according to equation (62). The value of the coefficients are compatible with estimates obtained from the Hamaker constants of the pure materials [83].

In order to describe the experimental finding, the description of the interface potential has been augmented by an additional (long-range) term, which decays like  $1/l^8$ . This term dominates  $g_{\text{exp}}$  at small distances and its strength has been adjusted to yield the measured contact angle of the polymer drops for each thickness of the coating layer. The form of the potential has a single minimum at short distances.

Using the sharp-kink approximation, we can calculate the monomer–substrate interactions which give rise to the interface potential above:

$$\frac{V_{\text{wall}}(z)}{\gamma_{\text{LV}}} = \epsilon_{\text{wall}} \left( \frac{1}{l^3} - \frac{r}{(l + d_{\text{ox}})^3} - \frac{c}{l^9} \right) \quad (64)$$

with  $\epsilon_{\text{wall}} = 2A/\phi_l$ . For the inaccuracy of the SCF calculations in predicting the interface tension not to upset the comparison with the experiment, we choose the strength of the monomer–wall potential  $V_{\text{wall}}$  such that the dimensionless ratio of the van der Waals contribution to the effective interface potential and the interface tension takes the experimental value. Using  $\epsilon_{\text{wall}} = 2A/\phi_l$  with  $A = 1.882 \text{ \AA}^2 = 0.069\sigma^2$ , we find  $\epsilon_{\text{wall}} = 0.167\sigma^5$ . The additional term  $l^{-9}$  in the interface potential could be (formally) conceived as a strong  $1/r^{12}$  attraction between the polymer segments and the constituents of the substrate, but it should be rather considered as an *effective* description of the attraction between the polymer and the substrate at short distances.

The monomer–wall potential (64) is appropriate for intermediate and large distances of  $l$ , which is the actual range of film thickness the dewetting experiments are able to probe. If we used equation (64) at all values of  $l$ , we would seriously underestimate the contact angle of the polymer drops on the substrate. Unfortunately, details of the monomer–wall potential at short distances are not known. We expect  $V_{\text{wall}}$  to be repulsive in the ultimate vicinity of the wall, because of the short-ranged repulsion (hard core interaction) between the polymer segments and constituents of the oxide layer. At short distances there is an attraction between the polymer segments and the wall. This contribution to the free energy is partially due to van der Waals interactions between polymer and oxide and partially due to specific interactions between PS and the  $\text{SiO}_x$  layer on the atomic scale. This short-ranged behaviour of  $V_{\text{wall}}$  cannot be modelled faithfully in the framework of our coarse-grained model: an accurate modelling of the liquid and the surface on the atomistic scale would be required.

As a minimal model we use the monomer–wall potential (64) up to distances where  $V_{\text{wall}} < -V_c$ . For smaller distances, we set  $V_{\text{wall}} = -V_c$  and  $\infty$  for  $z < 0$  (i.e. inside the oxide layer). The value of the contact potential  $V_c$  determines the contact angle of droplets on the bare substrate and the contact angle of drops on the mesoscopic film is rather independent from  $V_c$ . The values  $V_c$  are comparable to the attractive LJ interactions, but much smaller than the energy of a chemical bond ( $\epsilon_{\text{bond}} \sim \mathcal{O}(40\epsilon)$ ).

The dependence of the interface potential  $g(l)$  on the thickness of the oxide layer is shown in figure 11(c). Indeed, the interface potential exhibits two minima. A thin oxide layer ( $d = 9 \text{ \AA}$ ) cannot stabilize a mesoscopic film. There is a local minimum at mesoscopic thicknesses, but it is either unstable with respect to the minimum at  $l \approx 0$  or  $l \rightarrow \infty$ . The absence of a mesoscopic layer for a thin oxide layer is in accordance with previous observations [86]. Upon increasing the oxide layer, we stabilize a mesoscopic film and its layer thickness  $l^*$  grows with the oxide layer  $d_{\text{ox}}$ . This corresponds to the situation at high temperature. The thicker the oxide layer the smaller is the influence of the short-ranged contribution to the interface potential at  $l^*$ , and the more faithful follows the full interface potential of the long-ranged contribution  $g_{\text{exp}}$ . In fact, for a thick oxide layer ( $d_{\text{ox}} = 191 \text{ \AA}$ ), our calculations are by construction in good agreement with the mesoscopic film thickness  $l^* = 13 \pm 2 \text{ \AA}$  and the contact angle of  $7.5^\circ$  measured by Seemann *et al* [85].

## 7. Wetting on a polymer brush

Grafting or adsorbing chains to the substrate is another route to tune the wettability [87–90]. The grafted polymers may ‘tie down’ [88] the liquid film and prevent rupture. Their effect is two-fold: grafted chains might inhibit dewetting kinetically or they modify the interface potential as to form a thermodynamically stable wetting layer. We shall discuss only the latter effect and constrain ourselves to the most symmetric case of an oligomeric liquid on top of a chemically identical brush.

According to the Young equation [3] the polymer liquid will wet the brush if

$$\gamma_{BL} - \gamma_{BV} + \gamma_{LV} \leq 0. \quad (65)$$

Typically, the tension at the liquid–vapour  $\gamma_{LV}$  and brush–vapour  $\gamma_{BV}$  interface are large but of comparable magnitude, while the free energy cost  $\gamma_{BL}$  of the interface between brush and the free chain liquid is small. Hence, wettability is controlled by a subtle balance of all three contributions.

Much effort has been focused on the calculation of the surface tension  $\gamma_{BL}$  between the brush and the liquid, which stems from the interplay between the translational entropy the liquid gains by penetrating into the brush and the configurational entropy loss which follows when the chains of the brush are swollen by the free chains. Scaling considerations [91, 92] and SCF calculations [93–97] of incompressible melts with purely repulsive interactions have been applied with success to the manner in which a concentrated solution of free chains penetrate into the brush. At low grafting densities the penetration is large and  $\gamma_{BL}$  is negative; but there is little penetration at large grafting densities and  $\gamma_{BL}$  is positive. This dependence on the grafting density partially rationalizes the experimental observation that a polymer liquid does not wet a brush of identical monomers at high grafting densities [89, 98, 99]—a phenomena termed autophobicity.

The properties of the liquid–vapour or brush–vapour interface, however, cannot be described by models which invoke an incompressibility constraint and the effect of long-range van der Waals interactions between the liquid and the substrate is often neglected. In our SCF calculations we capture compressibility effects and can calculate all three interface tensions within a unified framework. In the following we illustrate the qualitative behaviour at temperature  $k_B T/\epsilon = 1.68$  and chain length  $N = 10$  using the MGM scheme (cf section). The average area per grafted chain is denoted as  $\Sigma$ . The first monomer of the grafted chains is placed a distance  $\Delta z = 1.2\sigma$  away from the wall, while free chains sample all spatial positions. In the following we discuss the wetting properties under conditions where the liquid coexists with its vapour in the bulk.

Three regimes of the reduced grafting density  $R_e^2/\Sigma$  can be distinguished:

- **Low grafting density.** In figure 12(a) we present the interface potential as a function of the average area  $\Sigma$  per grafted chain in the absence of long-range interactions  $A = 0$  (i.e. a hard repulsive wall). For low grafting densities the minimum of  $g(l)$  occurs close to the wall. In the absence of free chains the interface between the brush and the vapour resembles the liquid–vapour interface. There is a stable minimum of the interface potential close to the substrate. The film thickness which corresponds to this minimum is rather independent of the amount of grafted chains, but its depth decreases as we increase the grafting density. Free chains penetrate into the collapsed brush (cf figure 12(b)) but the attraction between the brush chains and the liquid is not strong enough to make the liquid wet the substrate. An attractive long-range interaction  $A > 0$  is necessary to bring about a first-order wetting transition at  $A_{\text{wet}}$ . As we increase the grafting density  $R_e^2/\Sigma$ , the wetting transition occurs at smaller values of  $A_{\text{wet}}$ . The dependence of the wetting transition on the grafting density is presented in figure 12(c).
- **Intermediate grafting density.** Upon increasing the grafting density further, the brush creates enough attraction to make the fluid wet the substrate at  $A_{\text{wet}} = 0$ . The line of first-order wetting transitions terminates in a critical end point (CEP). For larger grafting densities, wetting transitions are of second order, i.e. the thickness of the wetting layer increases continuously as the limit  $A \rightarrow A_{\text{wet}} = 0^+$  is approached. For negative values  $A < 0$  the liquid cannot wet the substrate, the contribution of the brush to the effective interface potential is short-ranged and cannot outweigh the long-range interactions

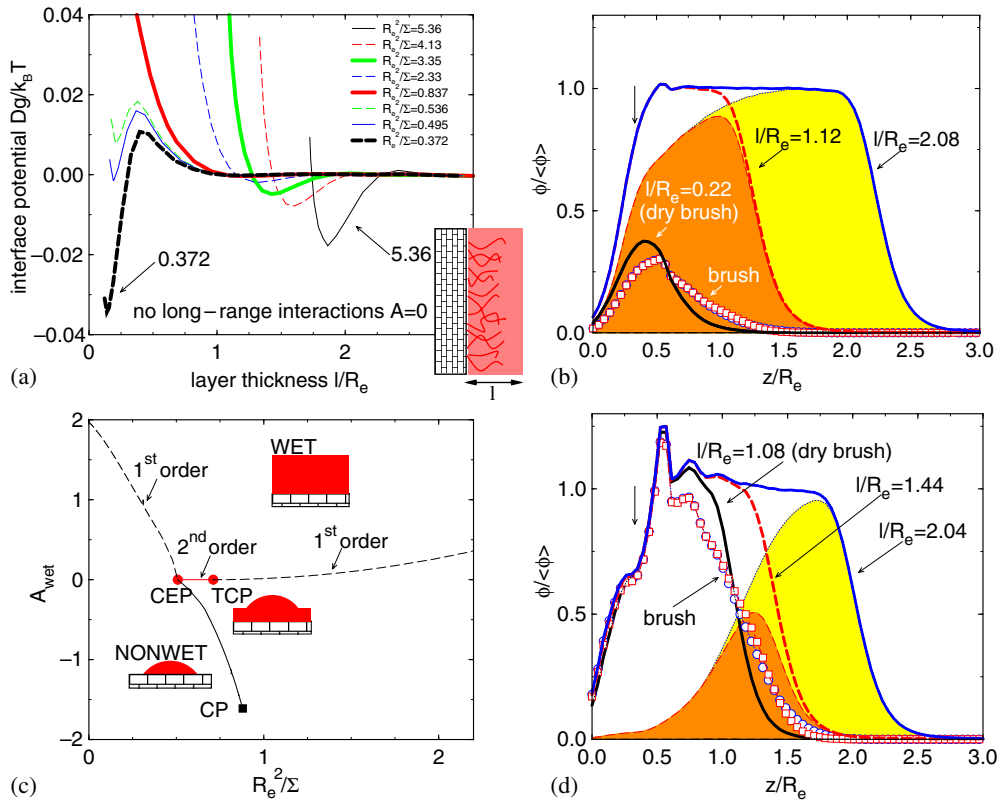


**Figure 12.** (a) Interface potential  $g(l)$  for various grafting densities  $R_g^2/\Sigma$  as indicated in the key. There are no long-ranged interactions ( $A = 0$ ) between the substrate and the monomers. (b), (d)) Density profiles at intermediate  $R_g^2/\Sigma = 0.69$  (b) and high  $R_g^2/\Sigma = 3.35$  (d) grafting densities. Film thicknesses are indicated in the key, the lowest value corresponding to a dry brush. The first monomers of the grafted chains are excluded from the profiles, their position is indicated by the vertical arrow. Thick curves present the total density profile  $\phi = \phi_g + \phi_f$ . For the two larger thicknesses, lines with symbols represent the profiles of grafted chains and shaded areas correspond to free chains. (c) Wetting phase diagram in terms of the effective Hamaker constant  $A_{\text{wet}}$  and the grafting density  $R_g^2/\Sigma$ . Broken curves denote first-order wetting transitions, the full curve denotes transitions between a microscopic thin and a mesoscopic thick layer, and the horizontal line at  $A_{\text{wet}} = 0$  marks second-order wetting transitions. The line of transitions between a thin and thick layer terminates in a CEP at low grafting densities and in a CP at high grafting densities. Second-order and first-order wetting transitions at high grafting densities are separated by a tricritical point (TCP) (from [40]).

for large (macroscopic) film thicknesses. The behaviour resembles the experimental observations (‘frustrated wetting’) of alkanes at the water–air interface [100–103]. The short-range interactions favour a thick liquid layer, but the long-range interactions  $A < 0$  inhibit the growth of a macroscopic liquid layer. The line of first-order wetting transitions at low grafting densities  $A_{\text{wet}} > 0$  continues into the regime of second-order wetting in terms of a transition between a microscopically thin and a mesoscopically thick layer at  $A_{\text{tt}} < 0$ . This behaviour is different from the prewetting behaviour, because it occurs at liquid–vapour coexistence  $\Delta\mu = 0$  and not at undersaturation  $\Delta\mu < 0$ . For  $A < A_{\text{tt}}$  a drop sits on top of a microscopically thin layer, while for  $A_{\text{tt}} < A < 0$ , the drop sits on top

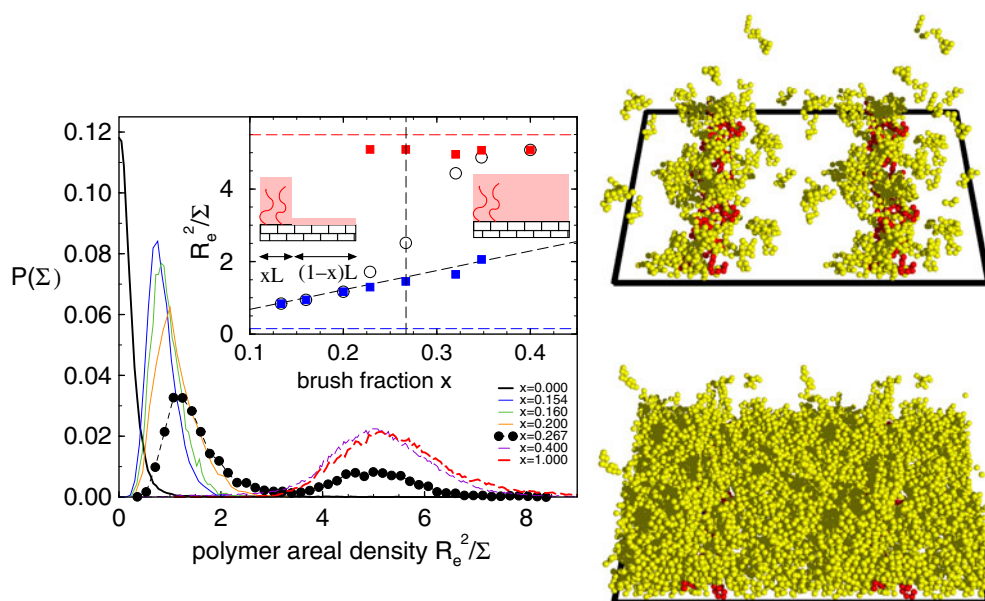


**Figure 13.** Probability distribution of the total thickness as a function of the fraction of the polymer brush  $x = L_B/(L_A + L_B)$  (cf sketch in the inset) at temperature  $k_B T\epsilon = 1.68$ ,  $\epsilon_w = 3.5$  and undersaturation  $\mu - \mu_{\text{coex}} = -0.15\epsilon$  (cf figure 10). Around  $x \approx 0.27$  there is a morphological transition. The broken curves mark the adsorption on the stripe, on the brush and the linear superposition. The panels on the right present snapshots of configurations at  $x = 0.266$ . The simulation box and three periodic images are shown. The upper and lower panels correspond to  $R_e^2/\Sigma = 1.38$  and  $5.67$ , respectively.

of a mesoscopically thick layer. Such a jump in the film thickness at coexistence which precedes the second-order wetting transition is also in agreement with the experiments of alkanes at the water–air interface [100, 101, 103]. The line of thin–thick transitions  $A_{\text{tt}}$  terminates in a CP at which the difference between the microscopically thin and the mesoscopically thick layer vanishes.

- **High grafting density.** Upon increasing the grafting density even further a stable minimum of the interface potential in the absence of long-range interactions  $A = 0$  develops. The larger the grafting density the deeper the minimum and the further away from the substrate it occurs. The density profiles at high grafting density are shown in figure 12(d). Adding a small amount of free chains we allow the collapsed chains of the brush to relax: in the absence of free chains the brush–vapour interface is similar to the very narrow liquid–vapour interface and a small amount of free chains allows the brush profile to adopt a broader profile which resembles the profile of a brush in contact with the liquid (melt). Unlike the situation at small and intermediate grafting densities, however, the free chains are expelled from the brush and confined into a narrow layer on top of the brush. Adding a small amount of free chains reduces the free energy initially. Increasing the amount of free chains beyond that necessary to relax the conformation of the brush chains, however, increases the free energy as the free chains are confined. This gives rise to the minimum in the interface potential. This minimum shifts to larger thickness as the grafting density is increased. Thus, in the absence of long-range attraction the liquid does not wet the dense brush of identical chains. This autophobicity has been observed on polymer brushes and crosslinked polymer networks. Upon making the substrate attract

the liquid  $A > 0$  we can overcome the autophobicity and make the liquid wet the brush. The wetting transition on the dense brush is of first order and  $A_{\text{wet}} > 0$  increases with grafting density.

Experiments [104] at intermediate grafting densities yield evidence for the stability of a thin and a mesoscopically thick film (at phase coexistence between the liquid and the vapour). More recently, experiments [105, 106] on the wetting of PS on a PS brush indeed observe two wetting transitions: at small and very large grafting density the polymer film dewets the brush, while at moderate grafting density the PS film remains stable.

## 8. Patterned surfaces

Another way to modify the wetting and adsorption properties is to exploit the influence of geometrical surface patterns. Bauer and Dietrich have investigated the wetting behaviour of a planar substrate containing a stripe [107–109]. This stripe consists of a chemically different material than the substrate. A particularly intriguing adsorption behaviour is found in the vicinity of the prewetting coexistence of the stripe material: at  $\Delta\mu < \Delta\mu_{\text{pw}} < 0$  the infinitely extended stripe is covered by a thin liquid layer, while for  $\Delta\mu_{\text{pw}} < \Delta\mu < 0$  a thick (but finite) layer builds up. Similar to capillary condensation, the transition between the thin and thick adsorption layers on the stripe is rounded-off, because the stripe is quasi-one-dimensional, and shifted away from the prewetting line of the infinite stripe. The magnitude of the shift depends both on the widths of the stripe and the adsorption properties of the substrate bordering the stripe [109]. Making the substrate more attractive to the fluid, one induces a change from a thin liquid layer adsorbed on the stripe to a thick film, and vice versa. This phenomena is termed morphological transition, because it implies a transition between two different density profiles (a snapshot showing the two different states is shown in figure 13).

In order to observe such a morphological transition in our MC simulations, we have to adjust the wetting properties of the stripe and the substrate carefully. In our simulations we use periodic boundary conditions in the two lateral directions such that we rather look at alternating stripes  $A$  and  $B$ . We work at temperature  $k_B T/\epsilon = 1.68$ , undersaturation  $\Delta\mu = -0.15\epsilon$  and use long-range attractions between the fluid and the wall according to equation (17) with  $\epsilon_w = 3.5$ . Under these parameters a thin liquid layer adsorbs on the stripe  $A$  (cf figure 11), and the stripe  $A$  is close to its prewetting transition. As second stripe  $B$  (or substrate), we use the same long-range attraction between the fluid and the wall, but we increase the fluid adsorption by grafting chains to the surface with  $R_e^2/\Sigma = 0.837$ . The SCF calculations in figure 12 suggest that the adsorbed amount on the brush  $B$  can be tuned easily, because the brush  $B$  exhibits a second-order or very weakly first-order wetting transition.

In the following we vary the width of the (first) stripe  $L_A$  and fix the width of the brush-covered second stripe to  $L_B = 8\sigma$ . In the inset of figure 13 we present the adsorbed amount per area as a function of the fraction  $x = L_B/(L_A + L_B)$  of the brush. For  $x < 0.2$  the adsorption increases linearly with the brush fraction. Around  $x \approx 0.27$  the average adsorption develops an s-shaped dependence on the brush fraction  $x$  and for  $x > 0.35$  the adsorbed amount on the patterned substrate almost reaches the value of the brush substrate. The average adsorption on the substrate is more than twice as much as the linear superposition would suggest. In the side panels we show two snapshots at the same brush fraction  $x = 0.26$ : in the upper snapshot, there is hardly any adsorption on the stripe  $A$  and the liquid condenses onto the brush-covered stripes  $B$ . The total adsorption is what one would expect by adding the adsorption on the stripe  $A$  and the brush  $B$  weighted by their areal fraction. In the lower snapshot, the liquid forms a uniform thick layer on the substrate and the total adsorption is comparable to the adsorption

on an infinitely extended brush  $B$ . The snapshots illustrate the two states separated by the morphological transition. As the system is two-dimensional (i.e. neighbouring stripes of the same type are coupled) the transition can be truly of first order.

During the simulation the system of finite size switches from one state to another. Therefore we do not observe a sudden increase of the adsorption at the morphological transition. It is instructive to look at the probability distribution of the adsorption. For small and large values of  $x$ , the distribution  $P(\Sigma)$  has a single peak centred around the average value of the adsorption. Close to the transition, however, the distribution is bimodal, each peak corresponds to the two states at the morphological transition. Around  $x \approx 0.27$  both peaks have equal weight and this criterion yields an estimate for the location of the transition. In the inset, we have also indicated the average adsorption which corresponds to the individual peaks: the lower value follows the weighted average of the stripe  $A$  and the brush  $B$ , while the higher value is close to the adsorption of the brush  $B$ . This gives an estimate for the adsorption one would observe in a larger system.

In order to study the ability of the stripe to modify the wetting behaviour of the substrate, it is interesting to compare the above results with similar adsorption simulation where the chains are grafted uniformly on the substrate, rather than forming stripes. For example, the stripe with areal fraction  $x = 0.267$  may be uniformly distributed to form a uniform brush with grafting density  $1/\Sigma = x/\Sigma_{\text{stripe}}$ . In this case we find that the stable state of the system consists of a thick layer of polymers, with total adsorption of  $R_g^2/\Sigma = 4.9$  polymers. It is interesting to note that a thin film is not stabilized, and that the adsorption of the stripe with equal amounts of grafted polymers is  $R_g^2/\Sigma = 5.1$ . This suggests that grafting polymers so as to form stripes may allow us to obtain larger absorptions than would be obtained if the polymers were uniformly distributed on the surface.

## 9. Summary and outlook

We have discussed MC methods and SCF calculations for studying the surface and interface properties of polymeric liquids. Both the structure (e.g. density profiles and chain conformations) as well as thermodynamic properties (e.g. surface and interface tensions) have been calculated accurately. Several versions of the SCF calculations have been quantitatively compared to the simulation results of a standard, coarse-grained polymer model. In the numerical SCF calculations the multichain problem is approximated by a single chain in an effective field. The properties of the single chain are calculated via a partial enumeration scheme, which takes due account of the chain conformations on all length scales. The effective interactions are described by a weighted density functional. For the theory to be quantitatively accurate, it is essential to decompose the density functional into a repulsive and an attractive part, with different approximations for the two parts.

Using both computational techniques we have investigated the wetting properties of our coarse-grained model at surfaces, which attract the fluid via long-range forces. Various methods of how to locate the wetting transition in the simulations have been discussed. The first-order wetting transition has been accurately located via the Young equation, and the concomitant prewetting line has been obtained.

We have explored how to modify the wetting properties:

- (i) The influence of a thin coating layer, which gives rise to an interplay between long-range and short-range forces, has been considered. This results in an effective interface potential with two minima, and leads in experiments to two distinct dewetting morphologies.
- (ii) Grafting chains to the surface results in a complex wetting behaviour, including first- and second-order wetting transitions.

- (iii) Chemically patterned substrates exhibit unusual adsorption properties which arise from a morphological transition.

These examples illustrate the versatility of the computational methods which allow a qualitative description of experimentally relevant systems. There are various other ways how to control the wettability of surfaces. Let us mention two examples:

- (i) Geometrical patterns, for instance wedges, can dramatically alter the wetting properties [110–112].
- (ii) The wetting properties might be tuned by surface active substances, like solvents or surfactants, which exhibit a preferential adsorption to the substrate or the vapour interface or surfactant.

Polymers offer an even larger range of possibilities: since the surface properties depend on the chemical composition in the very top of the substrate one can construct polymeric substrates with tunable surface properties using binary polymer brushes [113] or polymers which comprise segments with different surface properties [90].

Our calculations have been focused on the static wetting properties of coarse-grained models.

- (i) The kinetics of dewetting has attracted much interest. The SCF calculations can be extended to describe the dynamics. To date, however, only very simple SCF schemes, which use the Gaussian chain and simple, local interaction functionals have been used for dynamical calculations. A recent MC study investigated the spreading of microscopic droplets [114]. In the simulations only microscopically small droplets can be observed. On the one hand, much care has to be exerted to extrapolate the results to macroscopic drops (cf section 5.1.1). On the other hand, those microscopic droplets might exhibit new interesting behaviour which might be practically relevant for nanofluidic applications.
- (ii) In principle it is straightforward to include more details of the chemical structure in our calculations. In our partial enumeration scheme [115] we could use, for instance, chain conformations which have been obtained from atomistic simulations or the rotational isomeric state model [116].

A major challenge in this context is an accurate description of the interaction potentials. Information about the intermolecular potentials can be inferred from equation of state data and the long-range van der Waals interaction between the surface and the liquid can be parametrized by Hamaker constants. Much less is known about the interaction between the fluid and the substrate at short distance. As illustrated by the calculation on the wetting behaviour on an oxide-covered surface, changes of the order of  $k_B T$  per segment might lead to pronounced modification in the wetting behaviour.

### Acknowledgments

This work has benefitted much from fruitful and enjoyable collaborations with K Binder, Y-C Lin, P Müller-Buschbaum, M Stamm, O Wunnike and A Yethiraj. It is a pleasure to acknowledge stimulating discussions with C Bauer, S Dietrich, J O Indekeu, K Katsov, A Milchev, M Schick and R Seemann. Financial support was provided by the DFG in the framework of the priority program ‘wetting and structure formation at interfaces’ (Bi314/17). MM thanks the DFG for a Heisenberg stipend. LGM would like to thank Universidad Complutense and Ministerio de Ciencia y Tecnología for the award of a Ramon y Cajal fellowship and for financial support under contract BFM-2001-1420-C02-01. We gratefully

acknowledge ample access to the computing facilities at the NIC Jülich, HLR Stuttgart, and the computing centre of the University of Mainz.

## References

- [1] Schick M 1990 *Liquids at Interfaces (Les Houches Lectures)* (Amsterdam: Elsevier)
- Dietrich S 1988 *Phase Transitions and Critical Phenomena* ed C Domb and J L Lebowitz (New York: Academic) p 14
- Sullivan D E and Telo da Gama M M 1986 *Fluid Interfacial Phenomena* ed C A Croxton (New York: Wiley) p 45
- [2] Yethiraj A 2002 *Adv. Chem. Phys.* **121** 89
- [3] Young T 1805 *Phil. Trans. R. Soc.* **57** 827
- [4] Gretz R D 1966 *J. Chem. Phys.* **45** 3169
- [5] Dietrich S and Napiorkowski 1991 *Phys. Rev. A* **43** 1816
- [6] Indekeu J O 1992 *Physica A* **183** 439
- [7] Indekeu J O 1985 *Int. J. Mod. Phys. B* **32** 233
- [8] Gotta T and Dietrich S 1998 *Phys. Rev. E* **57** 655
- [9] Bauer C and Dietrich S 1999 *Eur. Phys. J. B* **10** 767
- [10] Kremer K and Grest G S 1990 *J. Chem. Phys.* **92** 5057
- [11] Benmennan C, Paul W, Binder K and Dünweg B 1998 *Phys. Rev. E* **57** 843
- [12] MacDowell L G, Müller M, Vega C and Binder K 2000 *J. Chem. Phys.* **113** 419
- [13] Siepmann J I 1990 *Mol. Phys.* **70** 1145
- [14] Frenkel D, Mooij G C A M and Smit B 1992 *J. Phys.: Condens. Matter* **3** 3053
- [15] Laso M, dePablo J J and Suter U W 1992 *J. Chem. Phys.* **97** 2817
- [16] Borgs C and Kotecky R 1990 *J. Stat. Phys.* **60** 79
- Borgs C and Kotecky R 1992 *Phys. Rev. Lett.* **68** 1734
- Binder K and Landau D P 1984 *Phys. Rev. B* **30** 1477
- [17] Müller M and Wilding N B 1994 *Phys. Rev. E* **57** 2079
- Müller M and Binder K 1994 *Comput. Phys. Commun.* **84** 173
- [18] Ferrenberg A M and Swendsen R H 1988 *Phys. Rev. Lett.* **61** 2635
- Ferrenberg A M and Swendsen R H 1989 *Phys. Rev. Lett.* **63** 1195
- [19] Berg B A and Neuhaus T 1992 *Phys. Rev. Lett.* **68** 9
- Berg B A, Hansmann U and Neuhaus T 1993 *Z. Phys. B* **90** 229
- [20] Wang J S, Tay T K and Swendsen R H 1999 *Phys. Rev. Lett.* **82** 486
- [21] Wang F G and Landau D P 2001 *Phys. Rev. Lett.* **86** 2050
- [22] Binder K 1982 *Phys. Rev. A* **25** 1699
- [23] Varnik F, Baschnagel J and Binder K 2000 *J. Chem. Phys.* **113** 4444
- [24] Müller M and MacDowell L G 2000 *Macromolecules* **33** 3902
- [25] Müller M and Werner A 1997 *J. Chem. Phys.* **107** 10764
- [26] Werner A, Schmid F, Müller M and Binder K 1999 *Phys. Rev. E* **59** 728
- [27] Werner A, Schmid F, Müller M and Binder K 1997 *J. Chem. Phys.* **107** 8175
- [28] Buff F P, Lovett P A and Stillinger F H 1965 *Phys. Rev. Lett.* **15** 621
- [29] Müller M and Schick M 1996 *J. Chem. Phys.* **105** 8885
- Müller M and Schick M 1996 *J. Chem. Phys.* **105** 8282
- [30] Milchev A and Binder K 2001 *J. Chem. Phys.* **114** 8610
- [31] Milchev A and Binder K 2002 *Europhys. Lett.* **59** 81
- [32] Fradin C *et al* 2000 *Nature* **403** 871
- [33] Mecke K and Dietrich S 1999 *Phys. Rev. E* **59** 6766
- [34] Romero-Rochín V and Percus J K 1996 *Phys. Rev.* **53** 5130
- [35] Wang S, Tolan M, Seeck O H, Sinha S K, Bahr O, Rafailovich M H and Sokolov J 1999 *Phys. Rev. Lett.* **83** 564
- [36] For a detailed discussion of the scattering intensity see e.g. Dietrich S and Haase A 1995 *Phys. Rep.* **260** 1
- [37] Müller M and Binder K 1998 *Macromolecules* **31** 8323
- [38] Adams P and Henderson J R 1991 *Mol. Phys.* **73** 1383
- [39] vanSwol F and Henderson J R 1991 *Phys. Rev. A* **43** 2932
- [40] Müller M and MacDowell L G 2001 *Europhys. Lett.* **55** 221

- [41] Woodward C E 1991 *J. Chem. Phys.* **94** 3183
- [42] Woodward C E and Yethiraj A 1994 *J. Chem. Phys.* **100** 3181
- [43] Patra C N and Yethiraj A 2000 *J. Chem. Phys.* **112** 1570
- [44] Sen S, Cohen J M, McCoy J D and Curro J G 1994 *J. Chem. Phys.* **101** 9010  
Sen S, Cohen J M, McCoy J D and Curro J G 1994 *J. Chem. Phys.* **102** 3431
- [45] Grayce C J, Yethiraj A and Schweizer K S 1994 *J. Chem. Phys.* **100** 6857  
Grayce C J and Schweizer K S 1994 *J. Chem. Phys.* **100** 6846
- [46] Müller M 1998 *Macromolecules* **31** 9044
- [47] Weinhold J D, Curro J G, Habenschuss A and Londono J D 1999 *Macromolecules* **32** 7276
- [48] de Gennes P G 1979 *Scaling Concepts in Polymer Physics* (Ithaca, NY: Cornell University Press)
- [49] Helfand E and Tagami Y 1972 *J. Chem. Phys.* **56** 3592  
Helfand E 1975 *J. Chem. Phys.* **62** 999
- [50] Noolandi J and Hong K M 1981 *Macromolecules* **14** 727  
Noolandi J and Hong K M 1982 *Macromolecules* **15** 483
- [51] Shull K R 1993 *Macromolecules* **26** 2346
- [52] Scheutjens J M H M and Fleer G J 1979 *J. Phys. Chem.* **83** 1619  
Scheutjens J M H M and Fleer G J 1979 *J. Phys. Chem.* **84** 178  
Scheutjens J M H M and Fleer G J 1985 *Macromolecules* **18** 1882
- [53] Matsen M W and Schick M 1995 *Phys. Rev. Lett.* **74** 4225
- [54] Szeleifer I 1997 *Curr. Opin. Colloid Interface Sci.* **2** 416  
Szeleifer I and Carignano M A 1996 *Adv. Chem. Phys.* **94** 742
- [55] Müller M 1999 *Macromol. Theory Simul.* **8** 343
- [56] Weeks J D, Katsov K and Vollmayr K 1998 *Phys. Rev. Lett.* **81** 4400  
Weeks J D, Vollmayr K and Katsov K 1997 *Physica A* **244** 461
- [57] Katsov K and Weeks J D 2001 *J. Phys. Chem. B* **10** 6738
- [58] Wertheim M S 1987 *J. Chem. Phys.* **87** 7323
- [59] Johnson J K, Zollweg J A and Gubbins K E 1993 *Mol. Phys.* **3** 591
- [60] Chapman W G, Jackson G and Gubbins K S 1988 *Mol. Phys.* **65** 1057
- [61] Stell G and Zhou Y 1989 *J. Chem. Phys.* **91** 3618
- [62] Stell G and Zhou Y 1992 *J. Chem. Phys.* **96** 1504  
Stell G and Zhou Y 1992 *J. Chem. Phys.* **96** 1507
- [63] Vega C, McBride C and MacDowell L G 2002 *Phys. Chem. Chem. Phys.* **4** 853
- [64] Flory P J 1954 *Principles of Polymer Chemistry* (Ithaca, NY: Cornell University Press)
- [65] MacDowell L G, Virnau P, Müller M and Binder K 2002 *J. Chem. Phys.* **117** 6360
- [66] Barker A and Henderson D 1967 *J. Chem. Phys.* **47** 4714
- [67] Carnahan N F and Starling K E 1969 *J. Chem. Phys.* **51** 635
- [68] Yethiraj A 1998 *J. Chem. Phys.* **109** 3269
- [69] Schweizer K S and Curro J G 1997 *Adv. Chem. Phys.* **98** 1
- [70] Müller M, MacDowell L G and Yethiraj A 2003 *J. Chem. Phys.* **118** 2829
- [71] Nordholm S, Johnson M and Fresier B C 1980 *Aust. J. Chem.* **33** 2139
- [72] Nath S K, McCoy J D, Donley J P and Curro J G 1995 *J. Chem. Phys.* **103** 1635
- [73] Donley J P, Rajasekaran J J, McCoy J D and Curro J G 1995 *J. Chem. Phys.* **103** 5061
- [74] Chandler D, McCoy J D and Singer S J 1986 *J. Chem. Phys.* **85** 5971
- [75] MacDowell L G, Müller M and Binder K 2002 *Colloids Surf. A* **206** 277
- [76] Binder K and Kalos M H 1980 *J. Stat. Phys.* **22** 363
- [77] Yang A J 1985 *J. Chem. Phys.* **82** 2082
- [78] Müller M, Binder K and Albano E V 2000 *Europhys. Lett.* **50** 724
- [79] Bruin S, Nijmeijer M J P and Crevecoeur R M 1995 *J. Chem. Phys.* **102** 7622
- [80] Nicolaidis D and Evans B 1989 *Phys. Rev. Lett.* **63** 778
- [81] Wilding N B 1995 *Phys. Rev. E* **52** 602
- [82] Hauge E H and Schick M 1983 *Phys. Rev. B* **27** 4288
- [83] Müller-Buschbaum P, Vanhoorne P, Scheumann V and Stamm M 1997 *Europhys. Lett.* **40** 655
- [84] Cazabat A M 1990 *Liquids at Interfaces (Les Houches Session Series)* ed J Charvolin, J F Joanny and J Zinn-Justin (Amsterdam: Elsevier) p 374
- [85] Seemann R, Herminghaus S and Jakobs K 2001 *J. Phys.: Condens. Matter* **13** 4925  
Seemann R, Herminghaus S and Jakobs K 2001 *Phys. Rev. Lett.* **86** 5534
- [86] Müller M, MacDowell L G, Müller-Buschbaum P, Wunnike O and Stamm M 2001 *J. Chem. Phys.* **115** 9960
- [87] Yerushalmi-Rozen R, Klein J and Fetters J L 1994 *Science* **263** 793

- [88] Reiter G, Schultz J, Auroy P and Auvray L 1996 *Europhys. Lett.* **33** 29
- [89] Liu Y, Rafailovich M H, Sokolov J, Schwarz S A, Zhong X, Eisenberg A, Kramer E J, Sauer B B and Satija S 1994 *Phys. Rev. Lett.* **73** 440
- [90] Yuan C, Ouyang M and Koberstein J T 1999 *Macromolecules* **32** 2329
- Jalbert C, Koberstein J T, Hariharan A and Kumar S K 1997 *Macromolecules* **30** 4481
- [91] Leibler L, Ajdari A, Mourran A, Coulon G and Chatenay D 1994 *Ordering in Macromolecular Systems* ed A Teramoto and T Norisuya (Berlin: Springer)
- [92] Gay C 1997 *Macromolecules* **30** 5939
- [93] Carignano M, Yerushalmi-Rozen R and Dan N 2000 *Macromolecules* **33** 3453
- [94] Ferreira P G, Ajdari A and Leibler L 1998 *Macromolecules* **31** 3994
- [95] Martin J I, Wang Z-G and Schick M 1996 *Langmuir* **12** 4950
- [96] Shull K R 1996 *Macromolecules* **29** 8487
- [97] Masten M W and Gardiner J M 2001 *J. Chem. Phys.* **115** 2794
- [98] Kerle T, Yerushalmi-Rozen R and Klein J 1997 *Europhys. Lett.* **38** 207
- [99] Jopp J and Yerushalmi-Rozen R 1999 *Macromolecules* **32** 7269
- Kerle T, Yerushalmi-Rozen R and Klein J 1998 *Macromolecules* **31** 422
- [100] Ragil K, Meunier J, Broseta D, Indekeu J O and Bonn D 1996 *Phys. Rev. Lett.* **77** 1532
- [101] Shahidzadeh N, Bonn D, Ragil K, Broseta D and Meunier J 1998 *Phys. Rev. Lett.* **80** 3992
- [102] Indekeu J O, Ragil K, Bonn D, Broseta D and Meunier J 1999 *J. Stat. Phys.* **95** 1009
- [103] Bertrand E, Dobbs H, Broseta D, Indekeu J, Bonn D and Meunier J 2000 *Phys. Rev. Lett.* **85** 1282
- [104] Maas J H, Cohen-Stuart M A, Leermakers F A M and Besseling N A M 2000 *Langmuir* **16** 3478
- [105] Vornov A and Shafranska O 2002 *Langmuir* **18** 4471
- [106] Maas J H, Fleer G J, Leermakers F A M and Cohen-Stuart M A 2002 *Langmuir* **18** 8871
- [107] Bauer C and Dietrich S 1999 *Phys. Rev. E* **60** 6919
- [108] Bauer C, Dietrich S and Parry A O 1999 *Europhys. Lett.* **47** 474
- [109] Bauer C and Dietrich S 2000 *Phys. Rev. E* **61** 1664
- [110] Parry A O, Rascón C and Wood A J 2000 *Phys. Rev. Lett.* **85** 345
- [111] Rejmer K, Dietrich S and Napiorkowski H 1999 *Phys. Rev. E* **60** 4027
- [112] Milchev A, Müller M, Binder K and Landau D P 2003 *Phys. Rev. Lett.* at press
- [113] Minko S, Müller M, Usov D, Scholl A, Froeck C and Stamm M 2002 *Phys. Rev. Lett.* **88** 035502
- [114] Milchev A and Binder K 2002 *J. Chem. Phys.* **116** 7691
- [115] Müller M and Schick M 1998 *Phys. Rev. E* **57** 6973
- [116] Flory P J 1969 *Statistical Mechanics of Chain Molecules* (New York: Wiley-Interscience)
- Mattice W L and Suter U W 1994 *Conformational Theory of Large Molecules: the Rotational Isomeric State Model in Macromolecular Systems* (New York: Wiley-Interscience)